IS-T 1755

Microstructural development of rapid solidification in Al-Si Powder

by

Jin, Feng

MS Thesis submitted to Iowa State University

Ames Laboratory, U.S. DOE

Iowa State University

Ames, Iowa 50011

Date Transmitted: September 26, 1995

PREPARED FOR THE U.S. DEPARTMENT OF ENERGY

UNDER CONTRACT NO. W-7405-Eng-82.

DISCLAIMER

TABLE OF CONTENTS

ABSTRACT

The microstructure and the gradient of microstructure that forms in rapidly solidificated powder were investigated for different sized particles. High pressure gas atomization solidification process has been used to produce a series of Al-Si alloys powders between 0.2 μm to 150 μm diameter at the eutectic composition (12.6 wt pct Si). This processing technique provides powders of different sizes which solidify under different conditions (i.e. interface velocity and interface undercooling), and thus give different microstructures inside the powders. The large size powder shows dendritic and eutectic microstructures. As the powder size becomes smaller, the predominant morphology changes from eutectic to dendritic to cellular. Microstructures were quantitatively charactrized by using optical microscope and SEM techniques. The variation in eutectic spacing within the powders were measured and compared with the theoretical model to obtain interface undercooling, and growth rate during the solidification of a given droplet. Also, nucleation temperature, which controls microstructures in rapidly solidified fine powders, was estimated. A microstructural map which correlates the microstructure with particle size and processing parameters is developed.

1. INTRODUCTION

In recent years, the powder processing of materials has become one of the important processing techniques to obtain a material with optimum properties. Because of the ability of these fine powders to solidify at a rapid rate, a variety of fine microstructures can be obtained which depend on the solidification rate of the powders. This rapid solidification process also can give a wide range of microstructures of stable/metastable phases. The undercooling conditions of powder processing play an important role in achieving these microstructures in the droplet.

Significant advances in powder processing have been made under rapid solidification conditions. Levi et al. [1, 2] examined heat transfer inside metal droplets and studied the relative roles of heat transfer, nucleation and growth on the evolution of microcrystalline structures in metal powders. The correlation between the two important solidification processing variables in powder processing (the size of the powder, and the cooling conditions in the chamber) and the microstructures have been only qualitatively developed, since the actual conditions under which fine powders solidify are very difficult to measure. The current knowledge of microstructures in fine powder is primarily based on experimental observations. Boettinger, Bendersky and Early [3] have mapped out various microstructures that form in undercooled droplets of Al-Fe as a function of particles size. Although these microstructures have been broadly related to powder size, significant variation in microstructure occurs within the powder. This variation in microstructures and the transitions in structures within a droplet have not been correlated quantitatively with the powder processing parameters.

Most recent studies on the rapid solidification process have been based on the theoretical models. The model of eutectic growth under the rapid solidification conditions has been developed by Trivedi, Magnin, and Kurz [4, 5]. Experimental studies on eutectic growth

have been carried out by Herlach and coworkers [6, 7, 8]. They carried out solidification studies in levitated droplets, and measured the solidification velocity V_r without external heat flow from heat balance during recalescence in an initially undercooled powder particle, and the growth rate V_e that was under external heat flow. Flemings et al. have examined the dendrite growth rate in undercooled melt under rapid solidification conditions [9]. They have been able to correlate the growth velocity with undercooling. Recently numerical studies of cellular structure growth have been carried out. The cellular and dendritic growth under rapid solidification conditons has been studied by Lu, Hunt, Gilgien and Kurz [10]. The relationship between the cellular spacing and solidification conditions at high velocities has been studied by Lu and Hunt [11]. These relations have been found to be analogous to those for the dendrite tip growth model. Only the operating parameter of cellular spacing is different. Rapid laser resolidification experiments of some alloys[12-15] have also been carried out and analyzed. All these previous studies confirm rapid solidification models which can thus be used to quantitatively analyze rapid solidification conditions inside the powders.

The goal of the present study is to examine the theoretical model and make critical experimental measurements that will clearly establish solidification conditions (i.e. interface velocity and interface temperature) that exist in powders not only as a function of powder size, but also as a function of time in a given particle. The following studies have been carried out: 1) The variations in the volume fraction of different microstructures with particle diameter, 2) the relationship between microstructure scales and powder particle size, 3) the variation of solidification conditions, such as interface velocity and interface undercooling, in a given powder size, 4) calculation of the coupled zone in undercooled Al-Si system to verify the predictions of this model with microstructure observations, 5) the nucleation region and nucleation temperature estimation, and 6) The micro-hardness test studies as a function of

powder diameter. The relations between powder hardness, powder particle size, and microstructures that include microstructure spacing and microstructure volume fraction have been obtained for the design of optimum processing conditions.

2. LITERATURE REVIEW

An extensive study of all literature pertaining to the rapid solidification of powder and the resulting microstructures was carried out. Relevant experimental studies and theoretical models will be used to analyze the solidification conditions in the atomization process.

2.1. Rapid Solidification Studies

Several experimental studies have been carried out to correlate microstructure with processing variables for atomized powders.

Boettinger, Bendersky and Early [3] have analyzed the microstructural characterization of aluminum alloy powder containing ~8wt pct Fe. Four distinct microstructures were found in the size range from 45 μm to 5 μm: microcellular α–Al; cellular α–Al; α–Al + Al_6Fe eutectic; and Al_3Fe primary intermetallic structure. The various microstructures as a function of powder diameter were mapped out from micrographs of these powders using the linear intercept method. The microstructures were broadly related to powder size. The effects of the internal heat flow and external heat flow were also discussed, but the variation in microstructure that occurs within the powder was not considered.

The evolution of heat flow, nucleation and growth in metal powders has been studied by Levi and Mehrabin [1, 18], who developed the solidification thermal history of undercooled spherical droplets. A mathematical formulation and solution methodology was developed for simulating the solidification process in an undercooled droplet from a single nucleation event occurring at its surface [1]. The thermal history of the aluminum droplets solidification was described by both a Newtonian and non-Newtonian fluids. The results of the interface velocity and undercooling as a function of particle size and the variation of the microstructures inside the powder with the thermal history were discussed.

In a companion paper [18], the microstructures of rapidly solidified aluminum alloy powders of submicron size was examined. This aluminum alloy powders were prepared by electro hydrodynamic (EHD) atomization process. The EHD process produced the powders smaller than 1 μm in diameter. Most studies were focused on the segregation in the Al-Si system, using alloys of 3 and 6 wt pct Si, as well as a high purity (99.999 pct) aluminum standard. The planar and cellular structures were observed, and the thermal history of solidification of these powders was shown to be described by the Newtonian model.

Flemings and coworkers have examined the dendrite growth rate in undercooled melt under rapid solidification conditions [9]. In this study, the solidification of undercooled Ni-25 wt pct Sn alloy has been observed by high-speed cinematography and compared with optical temperature measurements. This cinematographic measurements were carried out on samples undercooled from 68 to 146 K. The spacing of dendrites was on the order of millimeters. The growth front moved at measured velocities ranging from 0.07 meters per second at 68 K undercooling to 0.74 meters per second at 146 K undercooling. These velocities agreed well with the dendrite growth model of Lipton, Kurz, and Trivedi [19].

Herlach and Wei have measured eutectic growth velocities and undercoolings under rapid solidification conditions [6, 7]. These experiments were carried out in Co-25.5 wt pct Sb, Co-34.2 wt pct Sn, and Ni-5 wt pct Ag systems with a glass flux undercooling facility [20] under an 80 kPa He-20% H_2 atmosphere. The undercoolings were measured with a two-colour infrared pyrometer. An infrared photodiode device was designed to measure the recalescence time during rapid solidification. The velocities were taken as the ratio of sample size to recalescence time. The results were compared with the Trivedi, Magnin and Kurz model and Jackson and Hunt model.

2.2. Theoretical Models

The rapid solidification conditions of the powder can be examined by using several theoretical models. First, Newtonian thermal history model will be discussed.

2.2.1. Newtonian Thermal History Model

According to the Newtonian model, the thermal history of a cooling droplet can be described by [1]

$$(1+3Bi\Delta Fo)\theta_{k+1}+(\Delta c\theta_{k+1}-1)g_{k+1}-(\psi_k-1-3Bi\Delta FoSte)=0 \qquad (1)$$

where Bi =hr/k_L is the Biot number, Fo is the Fourier number or dimensionless time, Ste=$c_L(T_M-T_G)/\Delta H_M$ is the Stefan number, and the subscripts k and k+1 indicate the previous and current time steps, respectively, separated by an interval ΔFo.

A nucleation event in the form of a spherical cap is considered occurring at the droplet surface. The interface follows the axisymmetric geometry depicted in Figure 1. The fraction solidified is given by

$$g=0.5(1+Z^*)^3-0.1875(1+Z^*)^4 \qquad (2)$$

where (1+Z*) is the distance solidified along the growth axis.

$$\Delta Fo=\frac{Z^*_{k+1}-Z^*_k}{R} \qquad (3)$$

R=(r/α_L)V is the dimensionless interface velocity, r is powder radius, α_L is thermal diffusivity in liquid. V is velocity. The dimensionless enthalpy ψ and temperature θ are given by

$$\Delta c=(c_S-c_L)/c_L \qquad (4)$$

where c_L and c_s are the specific heats of the liquid and solid, the dimensionless enthalpy, $\psi=(H-H_{SM})/\Delta H_M$, and temperature, $\theta=c_l(T-T_M)/\Delta H_M$, H_{SM} and ΔH_M are the enthalpy of the solid and the heat of fusion at the melting temperature T_M.

For a given initial undercooling and partical size, the thermal history of this given powder can be obtained from above equations. Then the interface velocity and undercooling inside powder can be calculated.

During rapid solidification a great variety of microstructures can form. They are eutectic, dendrites, cells and planar front growth. These microstructures depend not only on the cooling conditions, but also on the alloy composition. From the current knowledge about composition and solidification conditions, the most important microstructures that appear in this Al-Si powder rapid solidification are eutectic, dendrites and cells. So these three microstructures will now be discussed.

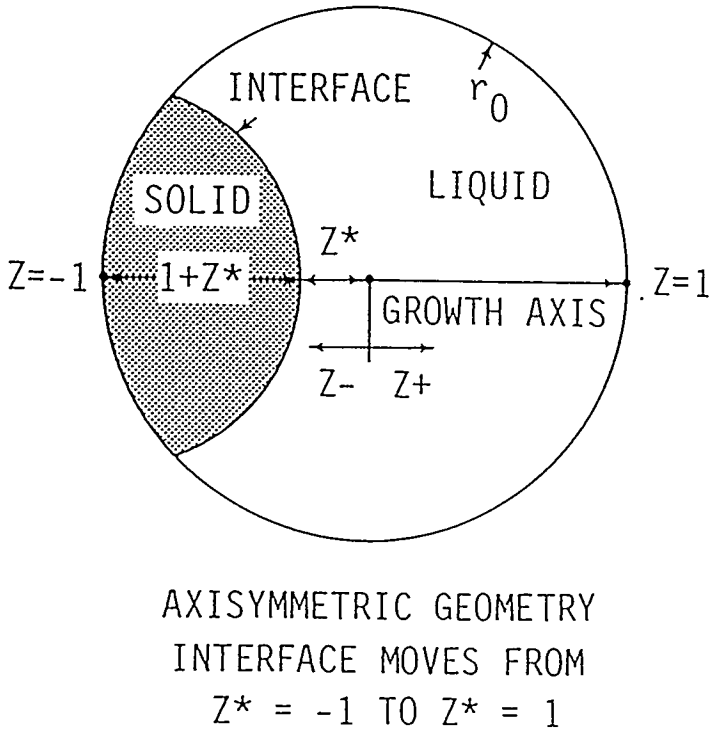

Figure 1. Interface geometry used for the Newtonian analysis of undercooled solidification from a single nucleation event [1].

2.2.2. Eutectic Growth Model

The eutectic microstructures are often distinguished into two growth morphologies: regular eutectic and irregular eutectic. In the regular eutectic, the interface is nearly planar so that both phases have about the same average undercooling at the interface. There are two types of the regular eutectic microstructures: lamellar and rod eutectics. In the irregular eutectic, the two phases have different average undercooling. The eutectic structure can be obtained under different solidification conditions which vary from low velocity to some critical high velocity. The theoretical models for eutectic growth have been developed by Jackson and Hunt [21] at low velocity and Trivedi, Magnin and Kurz [4] at high velocity.

1). JH model:

Assuming that the eutectic spacing, λ, is much smaller than the diffusion distance, D_L/V (where D_L and V are the solute diffusion coefficient in liquid and the eutectic growth velocity, respectively), and that the interface undercooling is sufficiently small so that the interface compositions are approximately the same as equilibrium compositions at the eutectic temperature, Jackson and Hunt have obtained the relationship between the undercooling, ΔT, the growth velocity, V, and the eutectic spacing, λ for regular eutectic growth:

$$\Delta T = K_c \lambda V + K_r / \lambda \tag{5}$$

Where K_r and K_o are system parameters, which have the following values [22]:

$$K_c = \frac{|m_\alpha||m_\beta|}{|m_\alpha| + |m_\beta|} \cdot \frac{C}{2\pi D} \tag{6}$$

$$K_r = \frac{2(1-f)|m_\beta|\Gamma_\alpha \sin(\theta_\alpha) + 2f|m_\alpha|\Gamma_\beta \sin(\theta_\beta)}{f(1-f)(|m_\alpha| + |m_\beta|)} \tag{7}$$

where m_α and m_β are the magnitudes of the α and β liquidus slopes at the eutectic temperature, C' is the difference in composition between the ends of the eutectic tie-line and C_β, D is diffusion coefficient in liquid, f is the volume fraction of α phase or β phase. Γ_α and Γ_β are the Gibbs-Thomson coefficient of α and β phases, and the angles θ_α and θ_β are shown in Figure 2.

This general solution of diffusion problem, given by equation (5), predicts that the eutectic spacing at a given growth rate depends on undercooling, as shown in Figure 3. Only those spacings which lie in the band $\lambda_m < \lambda < \lambda_M$ will be stable. The variation in λ_m with velocity was calculated by JH. For the minimum stable spacing they obtained the relations:

$$V\lambda_m^{\,2} = K_r / K_c \tag{8}$$

$$\Delta T\lambda_m = 2K_r \tag{9}$$

$$\Delta T / \sqrt{V} = 2\sqrt{K_r K_c} \tag{10}$$

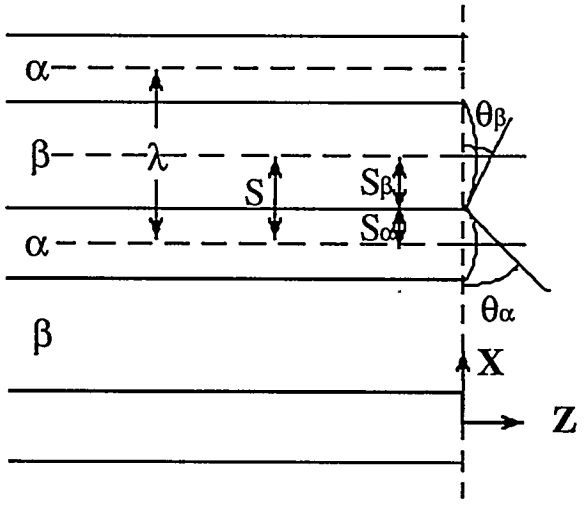

Figure 2. Schematic diagram of eutectic structure which defines the contact angles at the triple point junctions and eutectic spacing λ [21].

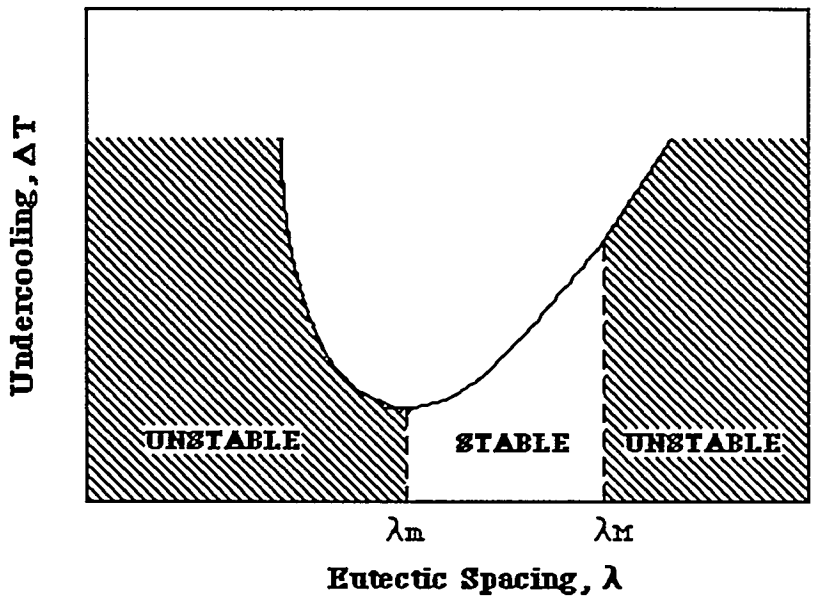

Figure 3. Relationship between the average interface undercooling and the eutectic spacing at a fixed velocity, and the regions of stable and unstable spacings [21].

Experimental studies have shown that the observed average eutectic spacing, λ, is large than λ_m. The deviation from λ_m is small for regular eutectic, where it is significant for irregular eutectic. If $\lambda/\lambda_m=\phi$, then one obtains:

$$V\langle\lambda\rangle^2 = \phi^2 K_r / K_c = \text{constant1} \tag{11}$$

$$\langle\Delta T\rangle\langle\lambda\rangle = (1+\phi^2)K_r = \text{constant2} \tag{12}$$

$$\langle\Delta T\rangle / \sqrt{V} = (\phi + \frac{1}{\phi})\sqrt{K_r K_c} \tag{13}$$

where the selection parameter, $\phi=\langle\lambda\rangle/\lambda_m$ [4].The value of ϕ is different for different systems. This model has been proven to be very successful for regular and irregular eutectics at low growth rates where the Peclet number, $P_e=V\lambda/2D_L$ is smaller than unity.

2). Trivedi, Magnin and Kurz model

Rapid solidification processing has challenged the JH eutectic-growth model. Because the solidification velocity can exceed 1 m/s, the diffusion distance becomes small, the undercooling becomes very large, and the Peclet number approaches unity, so that the two assumptions used by JH must be relaxed. Trivedi, Magnin and Kurz have extended the JH model to high growth velocity. The relations between eutectic spacing and solidification conditions for eutectic growth:

$$V\lambda^2 = a^L / Q^L \tag{14}$$

Where $Q^L = \left(\frac{C_0}{Df(1-f)}\right)[P + \lambda(\partial P / \partial\lambda)]$, For constant P(λ), this result is similar to that obtained by JH [21] (with a different value of P). However, the term in the large bracket of Q^L will cause $V^2\lambda$ to deviate from a constant value at high velocities. Also, if D varies significantly with undercooling, then $V\lambda^2$ will also deviate from a constant value. The magnitude of the large bracket is given by the expression:

$$P + \lambda(\partial P / \partial\lambda) = \sum_{n=1}^{\infty}\left(\frac{1}{n\pi}\right)^3 [\sin(n\pi f)]^2 \left[\frac{P_n}{1+\sqrt{1+P_n^2}}\right]^2 \frac{P_n}{\sqrt{1+P_n^2}} \tag{15}$$

$$\Delta T\lambda = ma^L\left[1 + \frac{P}{P + \lambda(\partial P / \partial\lambda)}\right] \tag{16}$$

This undercooling at the eutectic interface is equal to the JH result when P(λ) is constant.The eutectic model shows that by measuring λ, one can obtain the values of the interface velocity from equation (14) and the interface undercooling from equation (16).

2.2.3. Dendritic Growth Model

A dendritic structure is the most frequently observed structure in a solidified pure metal of alloy. "dendrite" comes from the Greek word "dendron" which means tree, and like a tree the dendrite is a branched structure with primary, secondary, tertiary, and eventually higher order branches. There are two distinctly different growth conditions which depend on the latent heat of fusion carrying away from the interface, Figure 4. They are : 1) Growth from an undercooled melt in which generally an equiaxed dendritic crystal forms, the latent heat of fusion being dissipated through the cooler liquid ahead of the interface. In this case the temperature gradient in the liquid at the interface is negative, whereas that in the solid is nearly zero. 2) Directional solidification or constrained growth in which a positive temperature gradient in the liquid is imposed so that the latent heat of fusion is dissipated through the solid. The dendrite growth direction and heat flow direction are parallel for solidification in the undercooled melt condition, whereas they are antiparallel in the directional solidification process. In an equiaxed crystal, the thermal and solute fields ahead of any given dendrite can be significantly influenced by the presence of other dendrites in neighboring grains [23]. Several important length scales are : dendrite tip radius, the primary spacing and the secondary arm spacing, as shown in Figure 5. For dendritic growth from an undercooled melt, the alloy composition C_0 and the undercooling ΔT, control the dendritic growth. The growth rate V, the tip radius R, and the secondary spacing λ_2 are important to quantitatively understand dendritic growth.

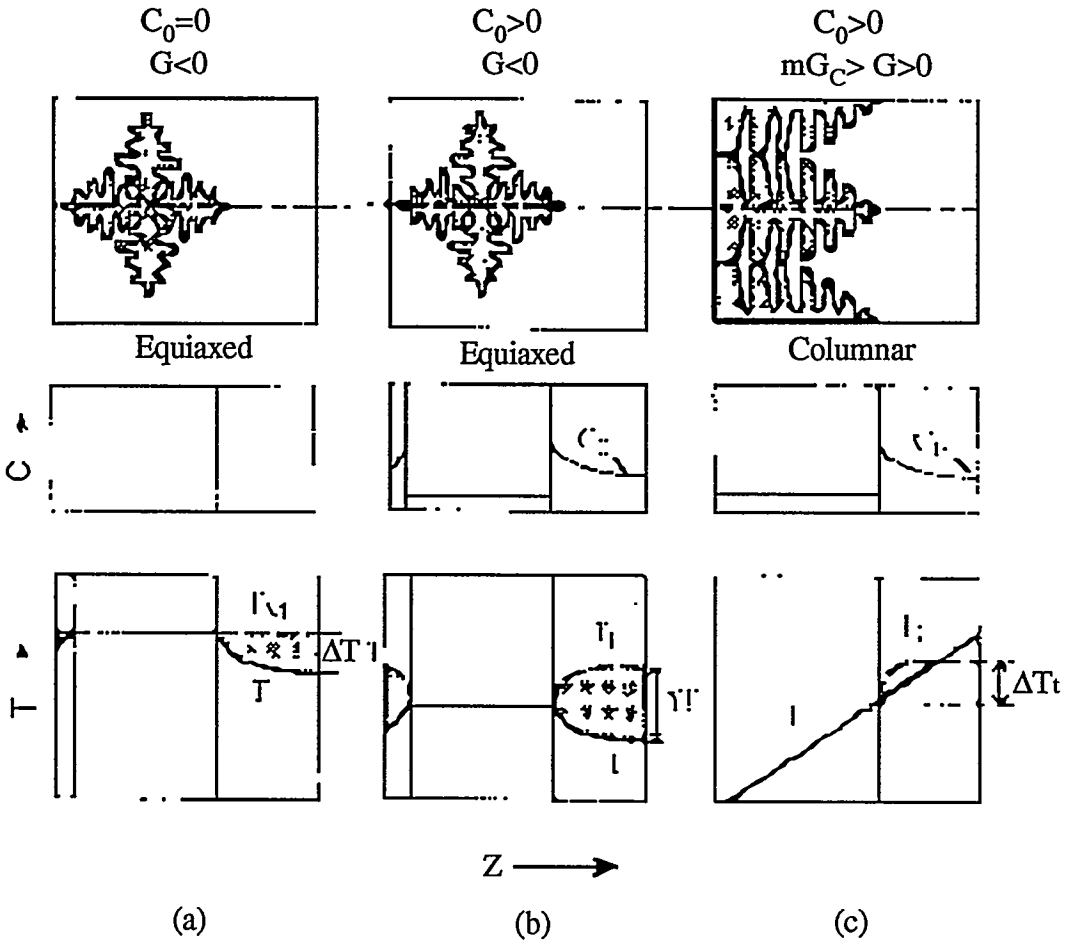

Figure 4. (a), (b) free growth and (c) constrained growth conditions: compositions and temperature fields are given along dendrite axis [23].

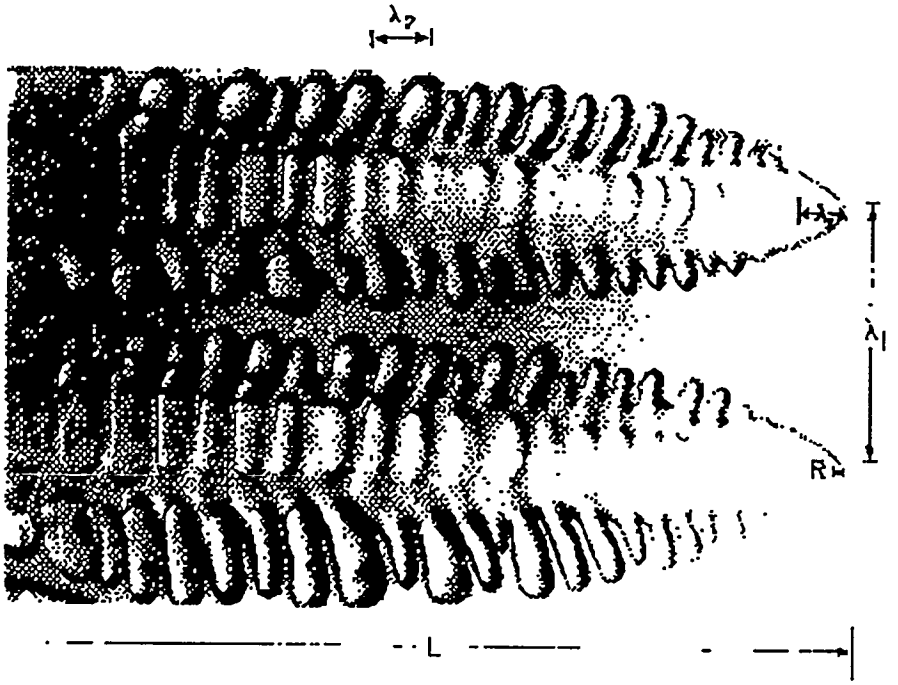

Figure 5. Important length scales of dendritic structure [23].

1) Dendritic growth in an undercooled melt

Significant studies in the dendrite tip selection process have been carried out [24, 25, 26]. The general dendrite tip radius selection criterion in an undercooled alloy melt as:

$$VR^2\left[\frac{k\Delta T_0}{\Gamma D}\right]\left[\frac{C_t}{C_0}\right]\xi_C + VR^2\left[\frac{\Delta H / c_1}{2\Gamma a_1 \beta}\right]\xi_1 = \frac{1}{\sigma^*} \qquad (17)$$

Where k is equilibrium distribution coefficient, $\beta=0.5[1+(K_s/K_l)]$, K_l and K_s are thermal conductivity of liquid and solid, ΔH is latent heat, c_L is volumetric specific heat of liquid, and $\Delta T_0=mC_0(k-1)/k$. σ^* is constant for most dendritic growth, $\sigma^*=0.025$.

The dendrite undercooling that relates the tip undercooling with the bath undercooling is given by:

$$\Delta T = \left(\frac{\Delta H}{c_L}\right) Iv(P_t) + \frac{k\Delta T_0 Iv(p)}{1-(1-k)Iv(P)} + \frac{2\Gamma}{R} \tag{18}$$

The function, $Iv(p)=Pexp(P)E_1(P)$, in which $E_1(P)$ is the exponential integral function. The variables P_t and P are the thermal and solute Peclet numbers of the dendrite tip, $P_t=VR/2a_L$ and P=VR/2D.

2) Dendritic growth in directional solidification

In directional solidification, where the melt is superheated, the undercooling is the dendrite tip undercooling ΔT_t. The dendrite tip temperature is primarily controlled by the solute diffusion[23]. The temperature gradient is imposed on the system by the process and the temperature gradient effect becomes important only at high velocities where latent heat contributions become significant. For directional solidification, the dendrite tip radius selection criterion and the dendrite tip undercooling can be expressed as:

$$VR^2\left[\frac{k\Delta T_0}{\Gamma D}\right]\left[\frac{C_t}{C_0}\right]\xi_C - GR^2 = \frac{1}{\sigma^*} \tag{19}$$

$$\Delta T_t = \frac{k\Delta T_0 Iv(p)}{1-(1-k)Iv(P)} + \frac{2\Gamma}{R} \tag{20}$$

The temperature gradient G is positive and the second term will be negative so that the thermal effect tends to stabilize the interface. The net driving force for destabilization is given by the difference in the two gradients, one due to the solute field and the other due to the temperature field. The left hand side of this equation represents the modified constitutional supercooling at the dendrite tip at low velocities where $\xi_C=1$. Also, at low velocities the latent heat effect is negligible and if the thermal conductivities, and thermal diffusivities in the solid and in the

liquid phases are the same, G=G1, the temperature gradient in liquid ahead of the tip, and one recovers the constitutional supercooling criterion. Note that the thermal gradient effects are negligible for dendrite tip undercooling at low velocities, although they may become important for the dendrite tip selection criterion at very high growth rates.

3). Rapid dendritic growth

The deviation of the functions ξ_i from unity in the dendrite tip selection criterion and nonequilibrium effects at the interface become important at high growth rates. Nonequilibrium effects are added into the equations (17, 18, 19, 20) so that the equations (17, 18) are modified as follows for rapid dendritic growth in an undercooled melt condition:

$$VR^2\left[\frac{k_v\Delta T_0^v}{\Gamma D}\right]\left[\frac{1}{1-(1-k_v)Iv(P)}\right]\xi_C + VR^2\left[\frac{\Delta H / c_1}{2\Gamma a_1\beta}\right]\xi_1 = \frac{1}{\sigma^*} \tag{21}$$

$$\Delta T = \left(\frac{\Delta H}{c_L}\right)Iv(P_t) + \left[\frac{k_v\Delta T_0^v Iv(p)}{1-(1-k_v)Iv(P)} + (m-m_v)C_0\right] + \frac{2\Gamma}{R} + \frac{V}{\mu_k} \tag{22}$$

The equations (19, 20) can be modified as follows for rapid dendritic growth in an directional solidification condition:

$$VR^2\left[\frac{k_v\Delta T_0^v}{\Gamma D}\right]\left[\frac{1}{1-(1-k_v)Iv(P)}\right]\xi_C - GR^2 = \frac{1}{\sigma^*} \tag{23}$$

$$\Delta T_t = \left[\frac{k_v\Delta T_0^v Iv(p)}{1-(1-k_v)Iv(P)} + (m-m_v)C_0\right] + \frac{2\Gamma}{R} + \frac{V}{\mu_k} \tag{24}$$

2.2.4. Cellular Growth Model

The cellular structure appears not only at low velocity but also at high velocity. Some time, the very fine cellular structures formed at high rates are called "microcellular" in order to differentiate them from the coarse cells that form at low rates. The cellular spacing, undercooling and tip radius as a function of velocity are shown in Figure 6 [10]. Numerical

studies of steady-state cellular growth have shown that cellular spacing at high velocities is similar to the dendritic growth model, i.e. R in equation (17) is replaced by λ and σ^* has a characteristic value for cellular growth. Thus, when cellular structures form, one can determine the value of V from the measurements of λ

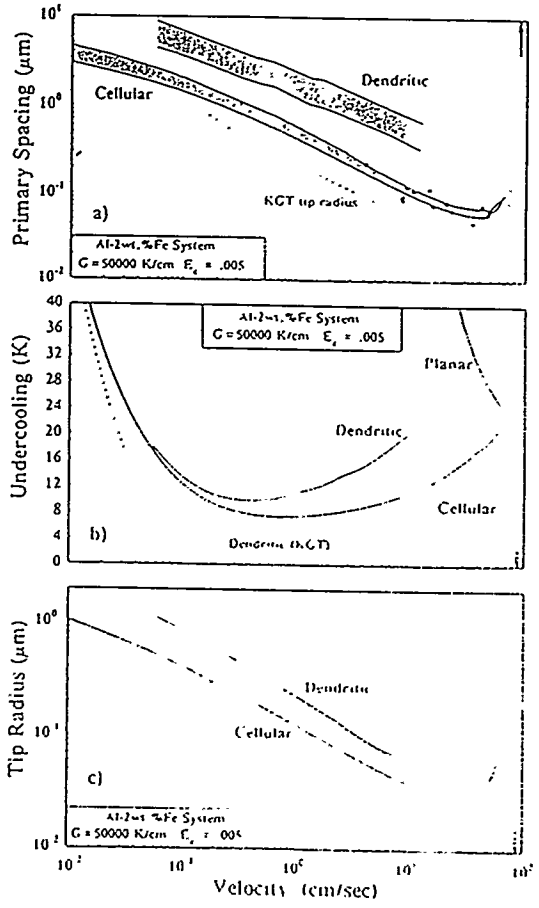

Figure 6. Spacing, undercooling and tip radii plotted against velocity for Al-2 wt% Fe. The filled circles are the experiment measurements from the laser resolidification experiments [6].

3. EXPERIMENTAL PROCEDURE

3.1. Materials and Preparation

3.1.1 Composition of droplets

The alloy powder was made by purity levels of 99.999% aluminum and 99.99% silicon powders. The composition for this alloys system was at the reported eutectic composition. This composition, as taken from the phase diagram is 87.4 weight percent aluminum and 12.6 percent silicon. The phase diagram for the aluminum-silicon alloys system is shown in Figure 7.

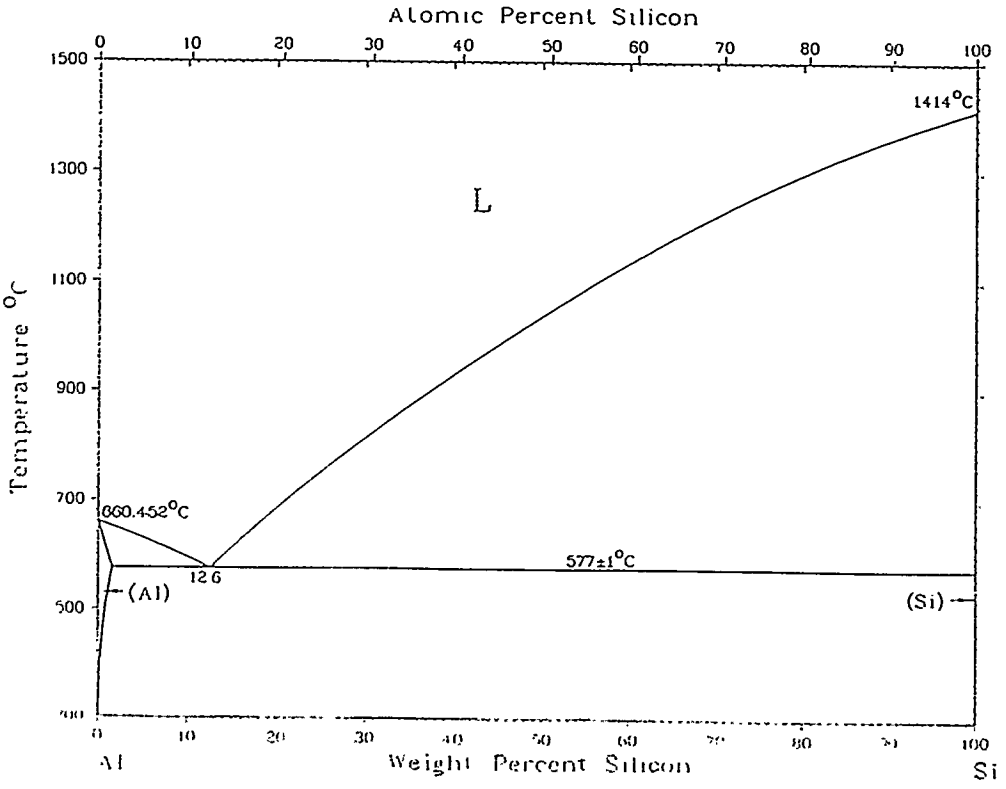

Figure 7. Al-Si phase diagram [34].

3.1.2 Gas atomization of droplets

This Al-Si alloy powder samples were prepared in high pressure gas atomization (HPGA) system. The HPGA is a method to use high pressure air, nitrogen, helium or argon as a fluid for breaking up a molten metal stream for efficient production of very fine metal and alloy powders [27]. Figure 8 is a schematic diagram of a vertical inert high pressure gas atomizer. For high temperature metals, a vacuum induction melter and a closed, inert gas-filled chamber are used to prevent oxidation.

In the alloy powder preparation procedure, the pure aluminum and silicon powders are mixed, and melted in vacuum induction melter that must be superheated. Then the plug is opened and the melt is poured into the nozzle. The discrete gas atomization nozzle can be described as follows, with reference to the terminology of Figure 9. First, as a melt stream enters the wake area of the high velocity gas flow at the melt feed tube tip, no extension of the cylindrical stream is projected into the atomization zone. Instead, as Figure 10 illustrates the melt forms a complete or partial film immediately on exit from the orifice and the film flows in a radial outward direction. The melt behavior in this base flow region is probably influenced both by a local subambient pressure effect, as great as about 0.5 atm below ambient [28], and by a strong recirculation flow which runs counter to the stream flow direction [29]. These complimentary effects cause the stream to split and fan outward and the resulting melt film to accelerate horizontally toward the external edge of the feed tube. A significant portion of the melt disintegration probably occurs when the melt film makes initial contact with the supersonic gas flow at the feed tube edge, as Figure 10 illustrates.

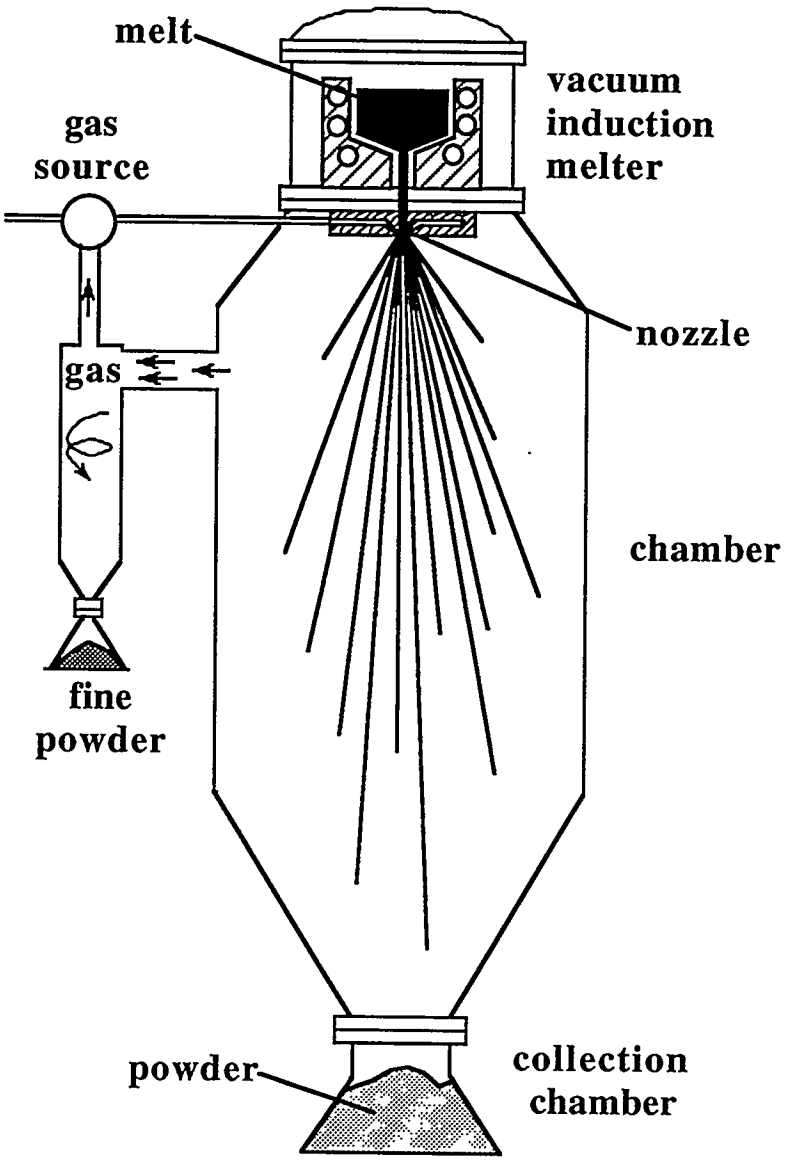

Figure 8. A vertical gas atomizer. The main features are a vacuum induction melter, gas expansion nozzle, gas recirculation and supply system, free-flight chamber, and powder collection chamber. An expanded view of the nozzle region is given to show the close proximity of the gas and melt streams needed for efficient atomization [31].

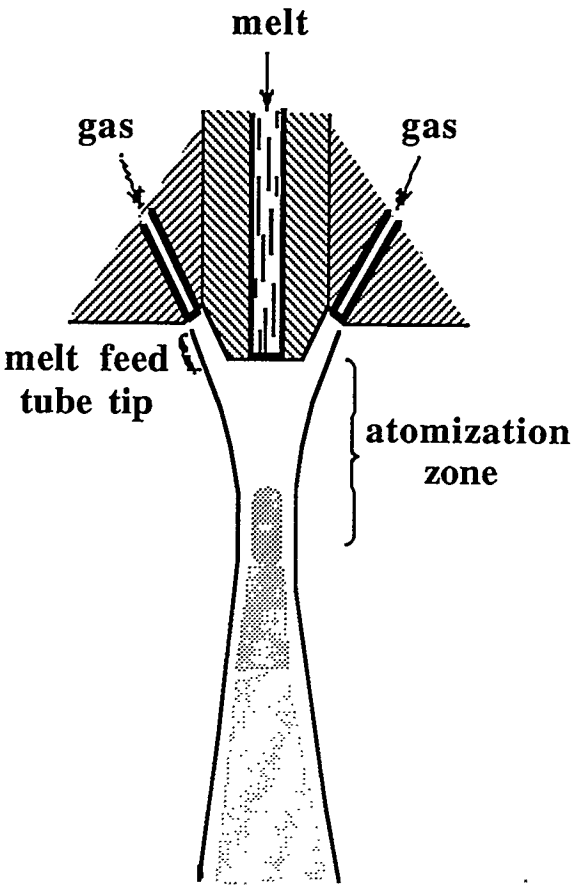

Figure 9. Schematic of high pressure gas atomization nozzle in a central cross-section view showing melt and gas feed relationships and nozzle terminology.

[Anderson, Morton and Figliola, 1989].

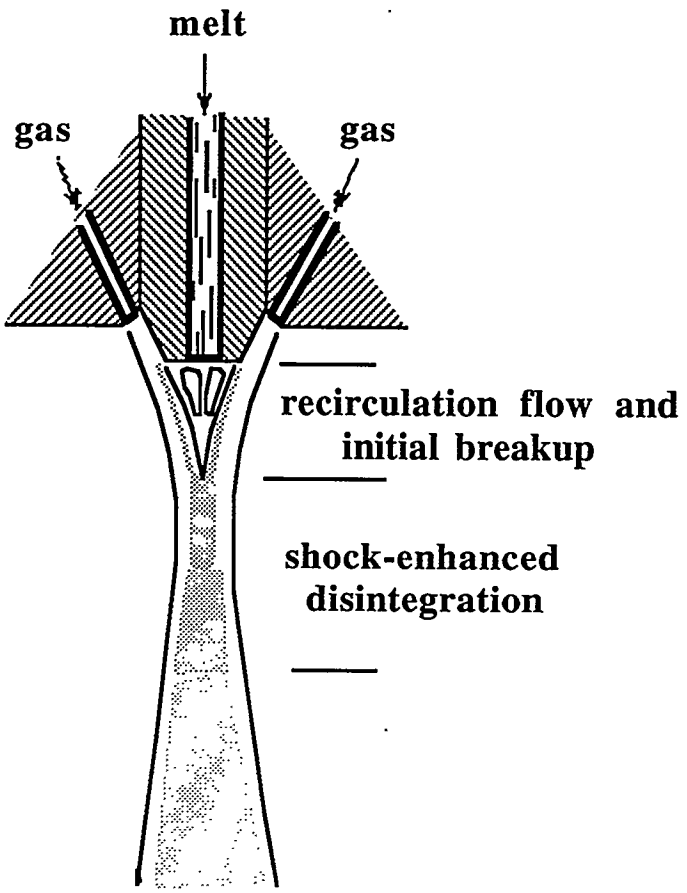

Figure 10. Schematic of droplet spray generation by gas atomization nozzle operating under HPGA conditions.

[Anderson, Morton and Figliola, 1989].

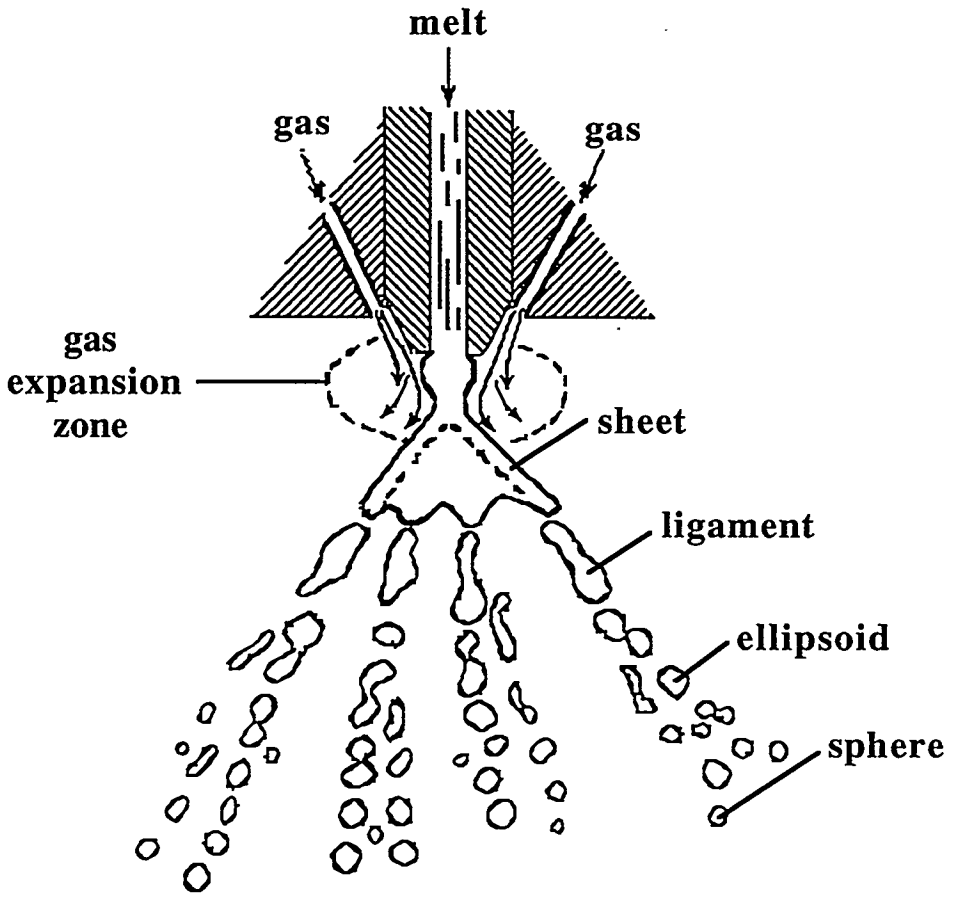

Figure 11. The formation of a metal powder by gas atomization involves the break-up of the liquid stream by the rapidly expanding gas. Because of a suction pressure in the gas expansion zone, the stream first forms into a thin hollow sheet, and subsequently forms ligaments, ellipsoids, and spheres [31].

Further disintegration and refinement of the droplets can also occur in the jet focus region at the bottom of the atomization zone as droplets are pushed through an intense normal shock front that has been observed at this location. The formation of a metal powder by gas atomization is shown in Figure 11. Downstream of the atomization zone the atomization gas flow entrains the fine droplets into a narrow spray cone which gradually broadens as the velocity decays. Solidification of the droplets occurs during free fall of this spray to produce very fine powder particles [30]. In the horizontal atomizer, the large filter area retains the powder while allowing gas to escape. For a contained system such as the vertical inert gas atomizer, it is necessary to incorporate a cyclone separator. The cyclone allows gas exit (and possible recycling) while leaving behind the fine particles. The chamber size must be sufficient to allow the largest particles to solidify before striking the walls.

Gas atomization can be performed totally under inert conditions, thereby maintaining the integrity of high alloy feedstock. The particle shape is spherical with a fairly wide size distribution. The gas atomization process has a large number of operating variables, including gas type, residual atmosphere, melt temperature and viscosity as it enters the nozzle, alloy type, metal feed rate, gas pressure, gas feed rate and velocity, nozzle geometry, and gas temperature. Those parameters are adjusted to maintain process control and tailor the powder characteristics for various uses. The experimental results showed that finer powders resulted from gas atomization at increased gas nozzle inlet pressures. In practice, gas atomization is capable of production rates as high as 100 kg/min [31]. The gas jet pressures are up to 28 MPa [29]. The main advantage of gas atomization is in the product homogeneity and the good packing properties available with the resulting spherical powder.

3.2. The Powder Separation

The diameter of atomized powder varied from 0.5 μm to 150 μm. For analysis these powders were separated according to particle size ranges.

3.2.1 Screening

Screening is a common technique for rapidly analyzing particle size. A square grid of evenly spaced wires creates a mesh. The mesh size is determined by the number of wires per unit length. Screen analysis begins with a stack of screens with decreasing mesh openings. The smallest opening size is at the bottom. The powder is loaded onto the top largest size screen and the screen stack is agitated for a period of time. The small powder passes through large size mesh. The large size powder is separated out. These Al-Si powder samples were carefully screened, using fine wire mesh sieves, and separated into four groups. The particle size of these groups were 150 μm ~ 88 μm, 75 μm ~ 63 μm, 44 μm ~ 38 μm, and 36 μm ~ 0.5 μm in diameter.

3.2.2 Sedimentation

From current knowledge, the most important microstructure changes were predicted to occur in group five. In order to obtain precise particle size of fine powders the finest group need to be classified in more detail. Sedimentation method was used to separate this smallest group.

Particles settling in a fluid (liquid or gas) reach a terminal velocity which depends on both the particle size and the fluid viscosity. Thus, particle size can be estimated from the settling velocity. According to the particle density and shape, sedimentation techniques are nominally applicable to particles in the 0.02 to 100 μm range [31]. From Stokes law, the terminal velocity of a sphere particle is

$$V = gD^2(\rho_m - \rho_f)/(18\eta) \quad (25)$$

Where g is gravitative acceleration (9.8 m/s^2 or 32.17 ft/s^2), D is particle diameter, ρ_m and ρ_f are densities of particle and fluid, η is fluid viscosity. For a given settling distance H, the settling time is

$$t = H/V \quad (26)$$

Obviously, the fastest settling particles are the largest while the smallest can take considerable time to settle. Two important conditions were required to settle these powder: 1) the settling solution can not react with aluminum or silicon at room temperature. 2) the viscosity of the settling solution is large enough to distinguish different size powder layer during sedimentation. Hexane (C_6H_{14}) just matches both of these conditions. The viscosity and density of C_6H_{14} are 0.33 cp (or 2.22×10^{-4} Lb/ft·s) and 0.6594 g/cm^3 (or 41.49 Lb/ft^3) respectively. The density of this Al-Si alloy is 2.65 g/cm^3 (or 167.06 Lb/ft^3). The H is the depth from liquid surface. Then, $V=1.01\times10^6D^2$(ft/s) or $3.114\times10^5D^2$(m/s).

Using above equations and parameters, the settling velocity V and the settling time that this size powder deposits from surface of settling solution down to distance H can be roughly calculated for a given particle diameter D. The powders are first mixed with settling solution in a small glass bottle, as shown in Figure 12. After mixing with settling solution, powder will deposit to the bottom of the solution. The different size powders have the different deposition velocity in the settling solution. The powders of diameter less than and equal to D, and top layer settling solution that is down to the settling distance H from the surface are taken out until the certain settling time is over. These powders are separated into two groups. One group diameter is larger than D, another group diameter is less than and equal to D. Hence, this method can be used to classify finer particle. This sedimentation method was used to separate the group four into 9 different size classes. The powder diameter of each group was determined

by optical microscope observation. First, a few powders were taken from each group and placed on a glass sheet. Then, these powder were observed under a microscope and photographed. The range powder diameter of each group was converted from the powder picture magnification. Table 1 shown the initial groups that were separated by screen, and Table 2 shown the finer groups that were separated group 4 into other 9 groups by sedimentation. Finally, these powders were classified into 12 groups.

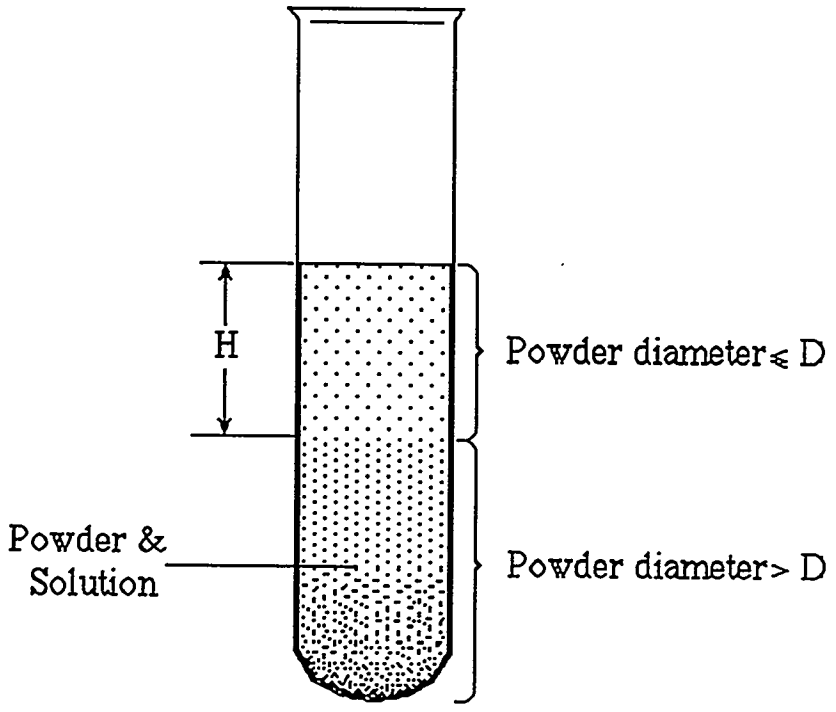

Figure 12. Powder sedimentation.

Group Number	Powder Diameter (μm)
1	150 ~ 88
2	75 ~ 63
3	44 ~ 38
4	36 ~ 0.5

Table 1. The four initial groups.

Group Number	Powder Diameter (μm)
1 (4)	36 ~ 34
2 (5)	34 ~ 28
3 (6)	30 ~ 24
4 (7)	26 ~ 18
5 (8)	18 ~ 14
6 (9)	16 ~ 12
7 (10)	14 ~ 10
8 (11)	12 ~ 8
9 (12)	8 ~ 0.5

Table 2 The 9 new groups that were separated from group 4.

3.3. Sample Preparation

The first step was to mount the powders for microscopic examination. Struers Epofix epoxy was chosen to mount the powder samples. This epoxy is a cold-setting resin based on two fluid epoxy components that were resin and hardener. Before mounting samples, 15 parts by volume of resin was mixed with 2 parts by volume of hardener for at least two minutes. The powder samples were mixed with the epoxy on a glass sheet and placed into a small plastic bottle, which was then evacuated to evaporate the bubbles. After at least 12 hours, the hard epoxy and powders were taken out from the bottle and placed in the mold. The epoxy mixture was poured in the mold and allowed to set for more than 12 hours. The sample was then polished by a polishing machine. The polishing procedure is from GRIT 600 (14 μm) to Linde B (0.05 μm) for each sample.

The etching solution was made from 15 ml HCL, 5 ml HNO_3, 5 ml HF (48%), and 7.5 ml H_2O. The polished sample surface was etched by this solution for couple of seconds (10s~6s). The etching time depends on the particle size. The big powder was etched a little longer than a small powder.

For scanning electronic microscope (SEM) observations, the sample was coated with carbon or gold to make it conductive. Because hundreds of powders were mounted in a sample by the above method, it was hard to distinguish and keep track of powder. For cross-section observations, the sample was prepared in a different way. First, a few powders were mixed with Hexane. Then, they were put on a carbon film by eye-drop. After drying, only a couple of powders were stuck on the carbon film. Finally, this carbon film and powder were mounted by epoxy, as shown in Figure 13.

Figure 13. The sample of powder put on film was used for powder cross section observation.

3.4. Microstructure Observation

3.4.1 Optical microscope observation

Optical microscope was used to observe the powder with diameter larger than 36 μm. The magnification of about 500X ~ 2,300X was used. The resolution is about 0.35 μm. The microstructures of powder were observed and photographed. The objectives of this observation were to examine: a). the microstructures in different size powders, and b). microstructures in the same size powder but with different cross sections.

3.4.2 SEM observation

When powder diameter is less than 36 μm, the fine microstructure of these powders can not be observed clearly. So scanning electron microscope (SEM) was used to observe these small powder samples.

The SEM is a type of electron microscope which produces unique, and often complementary, images and information. Comparing with the light optical microscope, the

SEM has greater resolving capabilities, as well as a wider and higher magnification range, usually between about 10X and 100,000X. In SEM the electron beam strikes the sample surface and the secondary electrons from the sample surface produce the image. The SEM requires operation under high vacuum conditions. Specimens for the SEM often require more extensive preparation than that needed for the optical microscope. Proper specimen preparation is critical to image quality, and therefore data acquisition, in SEM.

The SEM used in this powder observation were Cambridge S-200 and JEOL 6100 Scanning Electron Microscopy. The resolution of these machine are about 50 Å and 20 Å, respectively. The magnification ranges are about 10X ~ 30,000X and 10X ~ 100,000X. Both operate under vacuum below 10^{-6} torr. The operation voltages are 10 kv and 15 kv. The eutectic microstructure and nucleation region of powders were observed at the magnification between 2,000X and 16,000X, and photographed for the measurement of spacings.

3.5. Measurement

3.5.1 The measurement of the volume fraction of the microstructures

The linear intercept method was used to measure the volume percentages of cellular, dendritic, and eutectic structures from the optical and SEM microstructure pictures. First, a line was drawn on the powder microstructure surface. Then, the length of cellular, dendritic, and eutectic structures was measured on this line. The percentages of these structures were calculated. In the same direction, two other lines are drawn , measured, and calculated in the same way. Next, the three lines were drawn vertically. The percentages of the microstructures were measured and calculated as above. Finally, The average percentages of each structure were obtained. For one size powder, more than four different particles were measured.

3.5.2 The measurement of the microstructural spacing

Within the ranges of solidification conditions and composition used, a eutectic structure consisted of flake silicon in an aluminum matrix. The eutectic spacing was measured by using the procedure of Toloui and Hellawell (1976) described by Grugel and Kurz [32]. A line was drawn at right angles to parallel eutectic flakes on sections. The spacing, λ, was determined by L, the length of this line and n, the number of intercepts, as shown in equation (27) and Figure 2.

$$\lambda = \frac{L}{n} \tag{27}$$

The droplet distance is the length from nucleation region to a point along cells/ dendrites growth direction inside a powder. Measurements of eutectic spacing and cellular spacing as a function of distance were made in a given droplet.

3.5.3 The measurement of the hardness

The hardness of these powders were tested by micro-hardness machine. The particle sizes were from 120 μm to 20 μm. Because the smallest test prob size of this micro-hardness machine is 10 μm, the smallest powder that was tested by this machine is around 20 μm.

The samples were mounted with epoxy and polished to Linde B level. The cross sections of these powder were tested by using a load of 10 gmf (gram of force). The hardness value was determined by measuring the indenter mark on the surface of the powder cross section. The unit of the hardness was HV. For large powders, at least three hardness tests were carried out in each powder. For each size powder, at least four particles were tested. The hardness value of the epoxy was also tested. Because if the epoxy is not hard enough, the powder will cause deformation of epoxy during powder hardness test. The diamond hardness test mark on the powder surface is not very precise. The test hardness value of the powder may

be higher than real value, if the hardness of the epoxy has an influence on the powder hardness value, particularly for small particles.

3.5.4 The measurement of the particle size

The observed powder size can be roughly decided from pre-classification. But this diameter was not very precise. The method of precise diameter determination was carried out from the powder microstructure pictures. In this way, every measured powder must be close to at least one another powder that can be examined. The particles are illustrated in Figure 14. Because these powders have been classified by screen and sedimentation methods, the powder diameters are very close in each group. When some powders were mounted by epoxy, they almost deposited at bottom because of gravity. If a couple of powders were close together and at the same level, the real particle diameter cross-sections of these powders must touch side by side, as shown in Figure 14. This was the only way to determine the powder diameter since it is hard to determine isolated powder's diameter without successive sectioning.

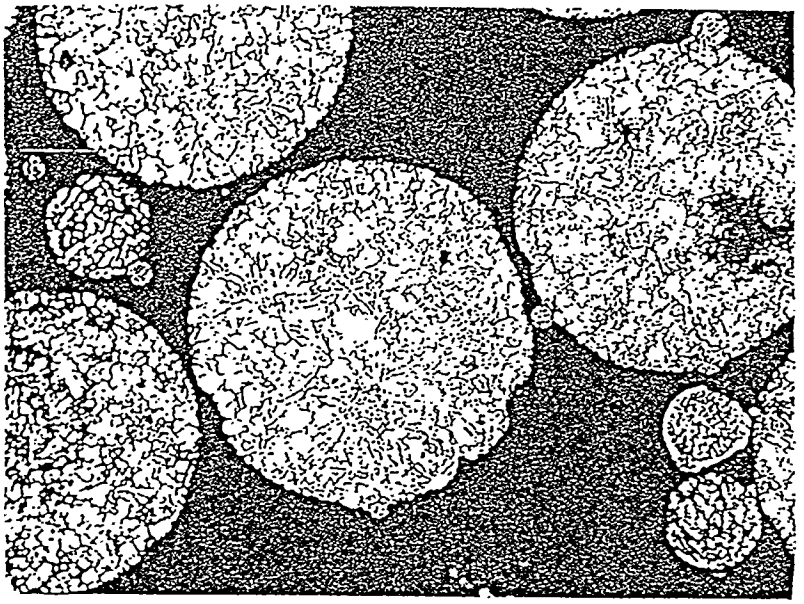

Figure 14. The determination of powder particle size.

4. EXPERIMENTAL RESULTS

4.1. Microstructures Transition Map

The volume fractions of cellular, dendritic, and eutectic microstructures as a function of powder diameter were characterized and shown in Figure 15. The observation of the microstructure was carried out from large powder to small powder. At the beginning, only the eutectic and dendritic structures were observed inside the powder. When powder size decreased to around 85 μm, the volume fraction of the dendritic structure equaled to the volume of the eutectic structure. The predominant morphology changed from eutectic to dendritic, as the powder size became smaller. The cellular structure appeared around 30 μm diameter powders. At that time, the volume fraction of dendritic structure began to decrease. The cellular structure had the largest volume fraction when powder diameter was less than 14 μm.

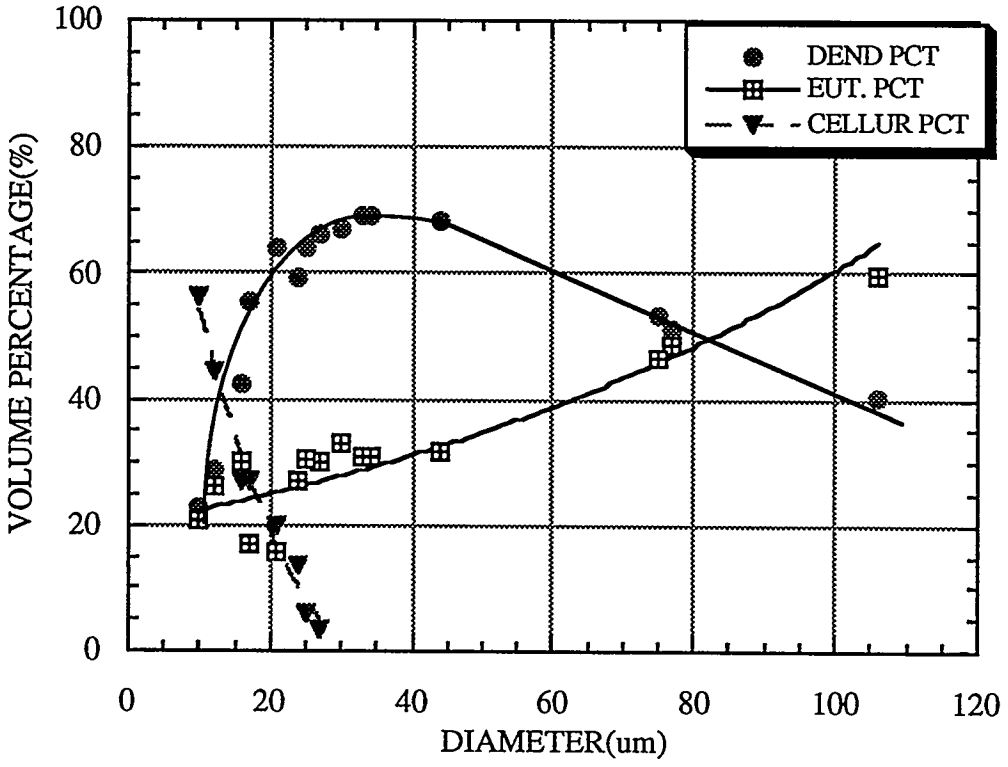

Figure 15. The Al-Si powder microstructures transition map.

4.2. Microstructural Spacing

4.2.1. The eutectic spacing in a given particle

Figures 16 and 27 show the microstructure of the solidified droplets of diameter 27 μm and 15 μm, respectively. Although the composition of the alloy corresponds to eutectic composition, both cellular and dendritic structures were also observed along with the eutectic structure. These structures became coarser as the solidification proceeded further away from the nucleation region. The eutectic spacing as a function of droplet distance is shown in Figure 18.

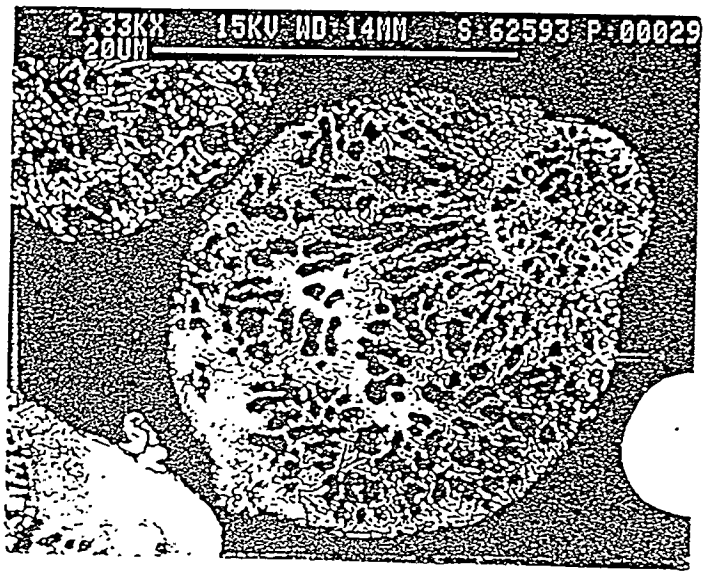

Figure 16. The microstructure of the solidified droplets of diameter 27 μm.

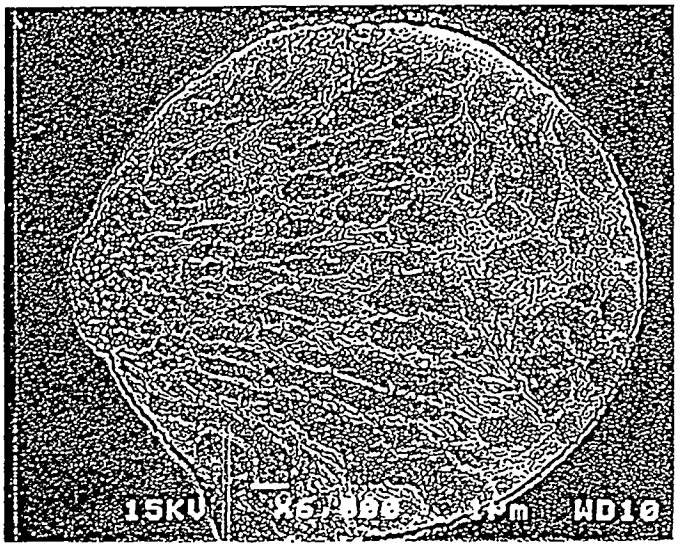

Figure (17). The microstructure of the solidified droplets of diameter 15 μm.

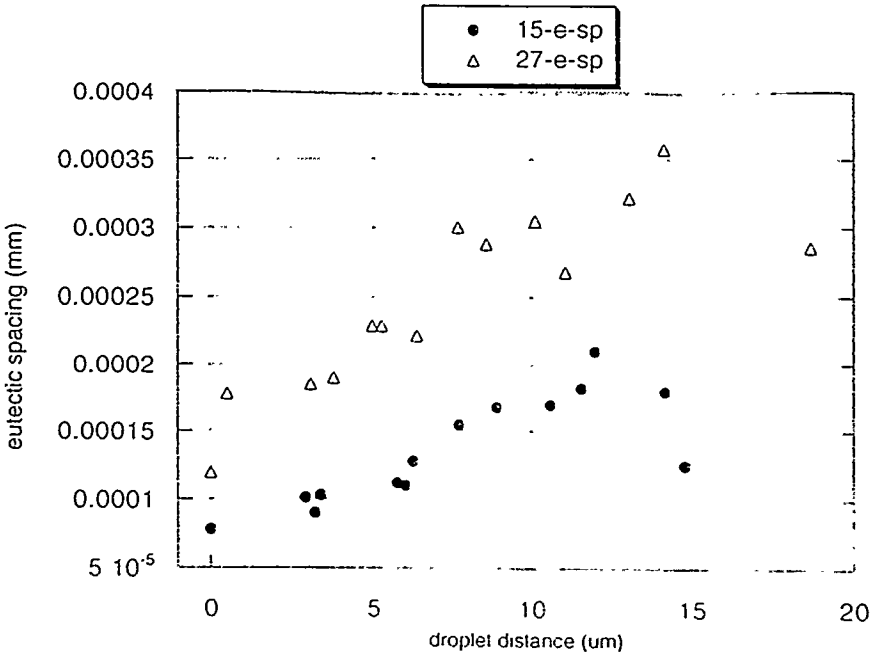

Figure 18. The eutectic spacing as a function of droplet distance with diameter 27 μm, and 15 μm size powders.

4.2.2 The eutectic spacing in whole range of powders

Figure 19 shows the microstructures of different size powders. The spacings of the eutectic structure are different in whole range of powders. The eutectic structure between the dendritic and cellular was measured. As particle size decreases, the eutectic spacing decreases. As Figure 18 shown, the eutectic spacing also changes inside powders. So for each size of particle, a range of eutectic spacing can be measured. The average eutectic spacing as a function of powder diameter is shown in Figure 20. The maximum and minimum eutectic spacing are also shown in this figure.

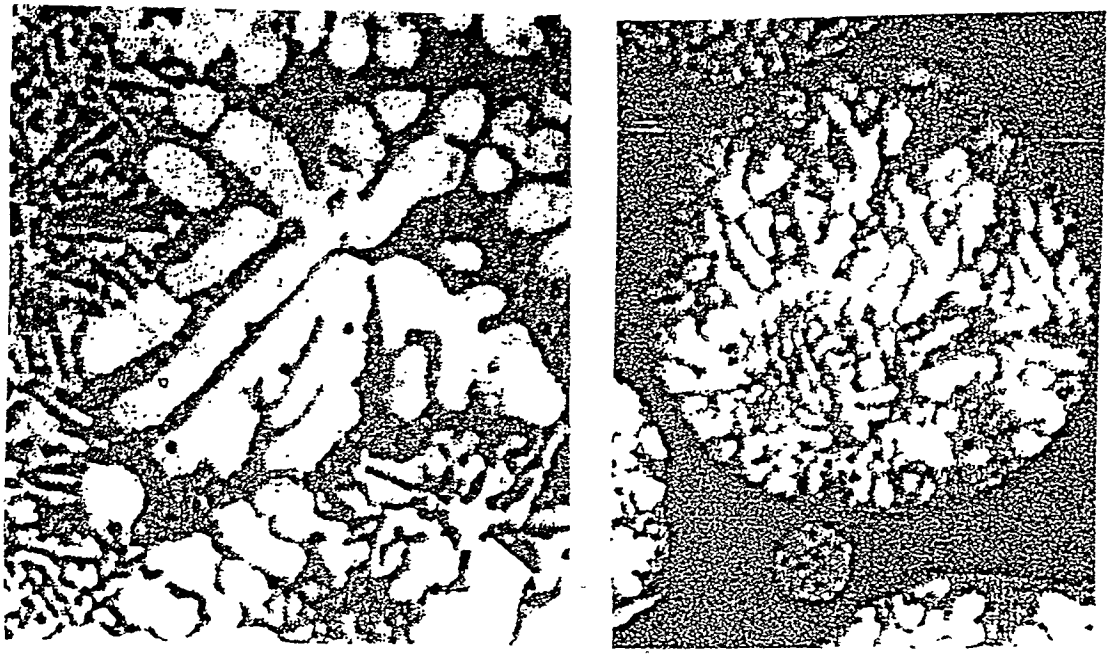

a b

Figure 19. The microstructures of different size powders, (a) powder diameter is around 70 μm (X2600), (b) the diameter of the powder is around 18 μm (X2600).

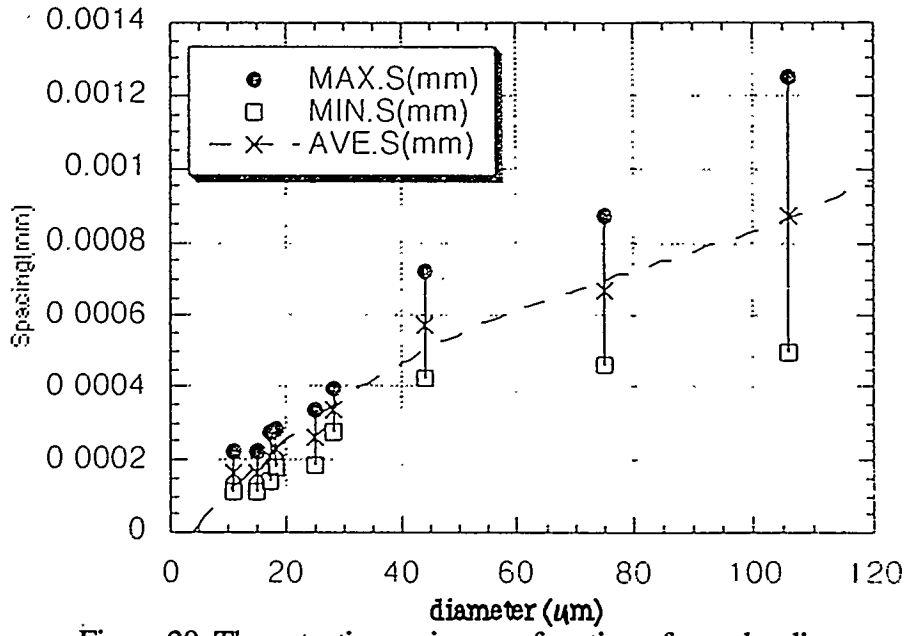

Figure 20. The eutectic spacing as a function of powder diameter.

4.2.3 The changing of the cellular spacing

Not only the eutectic spacing but also the cellular spacing are function of the droplet distance and the particle size. The fine cellular spacing was found near the nucleation region. The cellular spacing became coarser as the solidification proceeded further away from the nucleation region. The cellular spacing as a function of droplet distance is shown in Figure 21. The cellular spacings of whole range of powder are also different. Actually, the cellular structure first appeared in particle size around 30 μm. As particle size decreasing, the average cellular spacing decreased. Figure 22 shows the average cellular spacing changing from 30 μm to 10 μm.

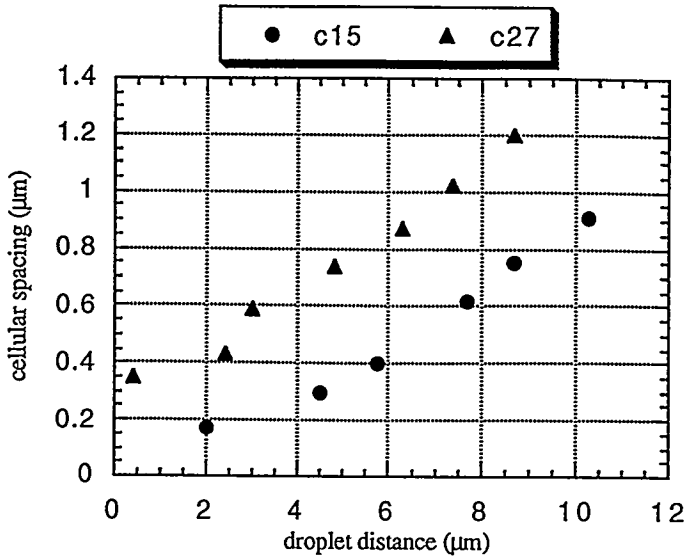

Figure 21. The cellular spacing as a function of droplet distance inside 27 μm size powder and 15 μm size powder.

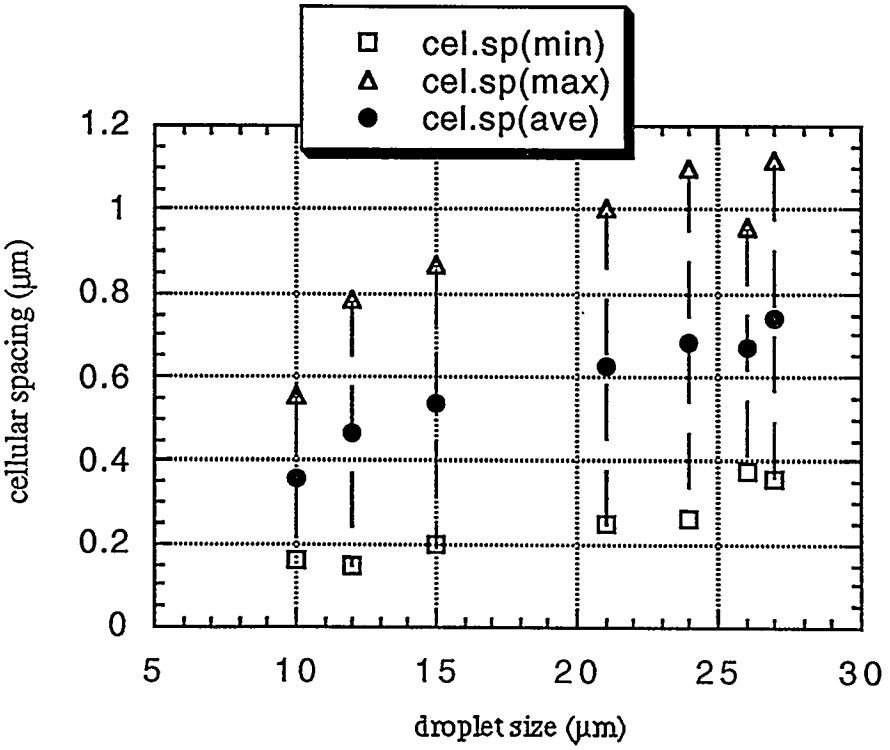

Figure 22. The cellular spacing as a function of particle size.

4.3. Powder Hardness

The hardness value as a function of powder particle size is shown in Figure 23. The highest hardness value was around 75 HV, found at large powder. The hardness decreased as particle size decreasing. When powder size decreased to 36 μm, the lowest hardness value was found. It was around 45 HV. If continually decreasing the powder diameter, the hardness value began to raise. The epoxy that was used to mount the powder must have some influence on powder hardness test, particularly on small particles. The epoxy hardness was around 17 HV.

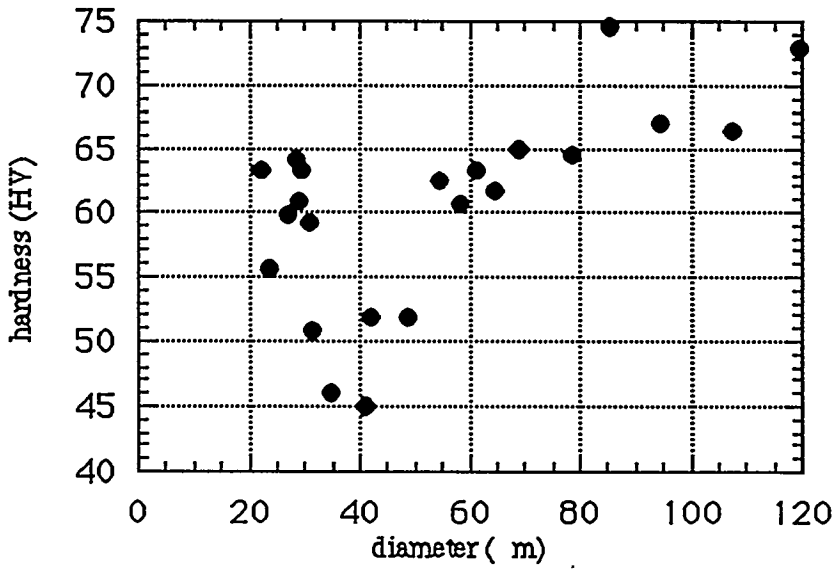

Figure 23. The powder hardness as a function of particle size.

4.4. Cross Section Microstructure

For determination of nucleation region, the cross sections of a given powder were observed layer by layer. The powders of diameter 19 μm, 11.5 μm and 10 μm were observed by optical microscope. The cross section pictures of these powders are shown in Figure 24, 25. There were dendritic, cellular, and eutectic structures at the top layers, as shown in Figure

24 (a-f) and Figure 25 (a-c). When the cross sections of these powders were polished to the layers that are shown in Figure 24 (g) and Figure 25 (d), the nucleation regions appeared in area A. The dendritic and cellular crystals growth direction were from point A to far away from these nucleation regions. After polishing to the bottom layer, the nucleation region disappeared, Figure 24 (k, l). Two types nucleation region, as shown in Figure 24 and Figure 25, were observed. One type solidifies at one or more points and crystal grows continually from these points. The nucleation region in this kind of droplet is shown as the area 'A' in Figure 24 (g). Another type solidified around these small particles and crystal grows from the surface of small particles. The nucleation region is shown as the area 'A' in Figure 25 (d).

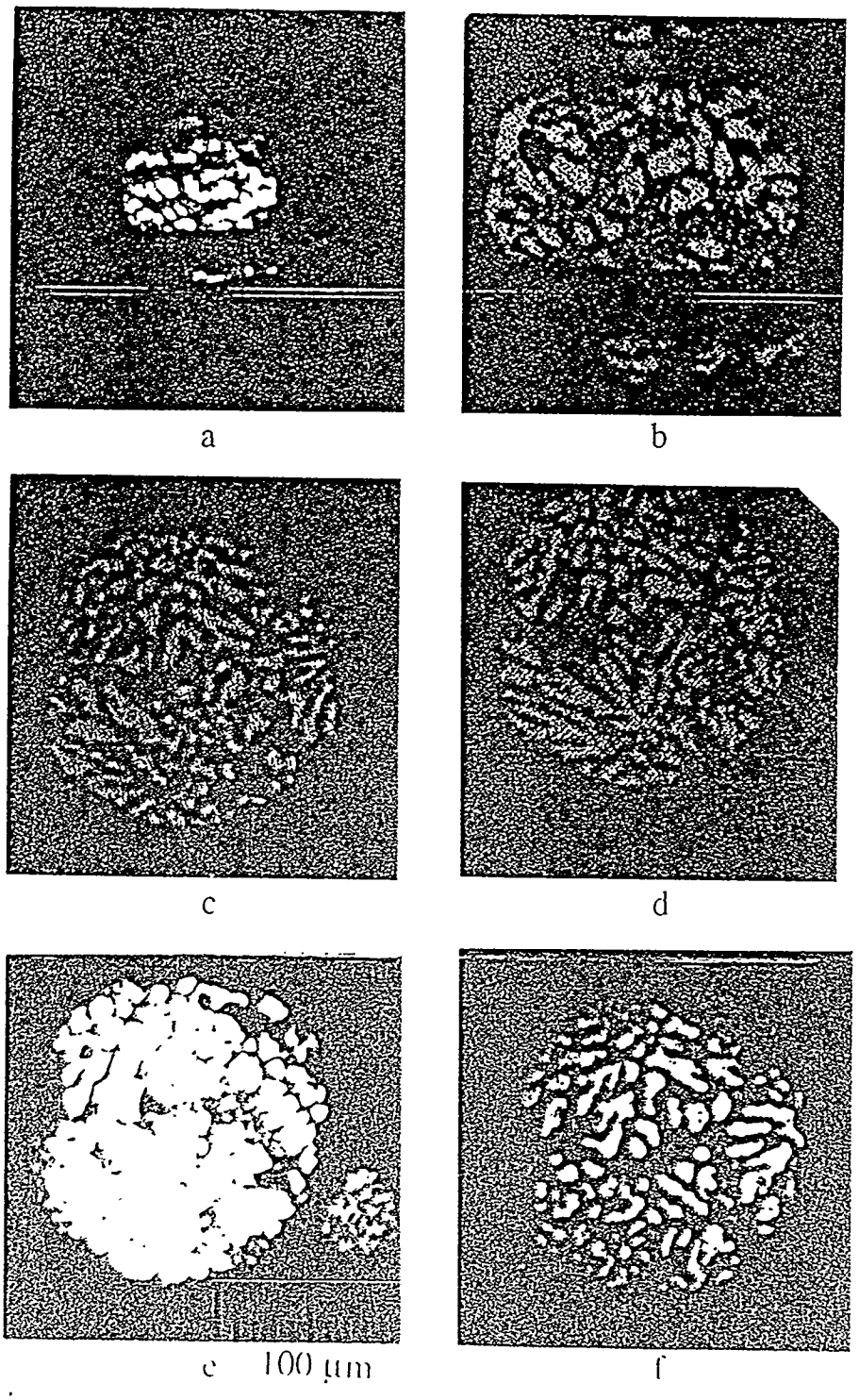

Figure 24. The cross section pictures of powder size 19 µm.

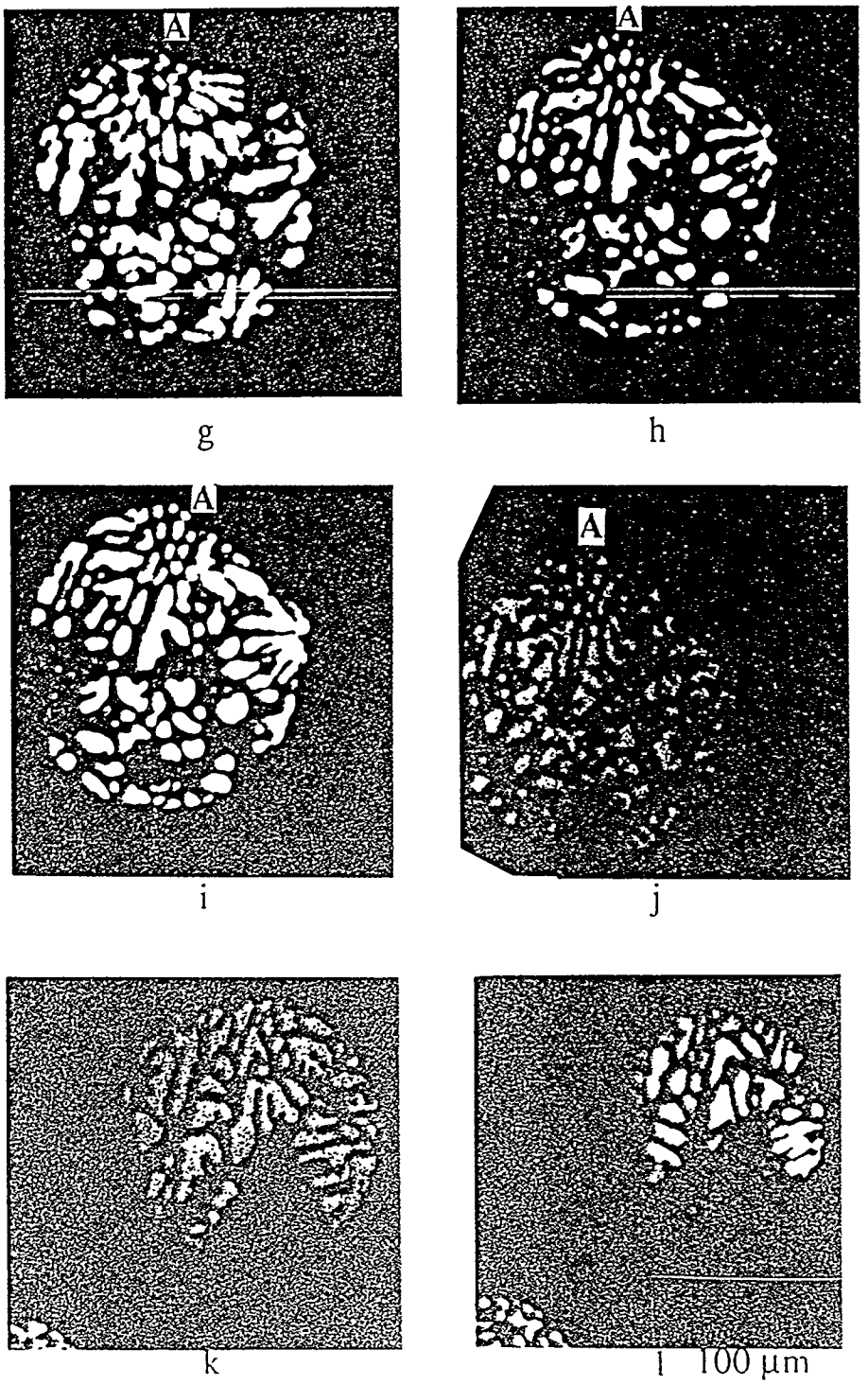

Figure 24. (continued).

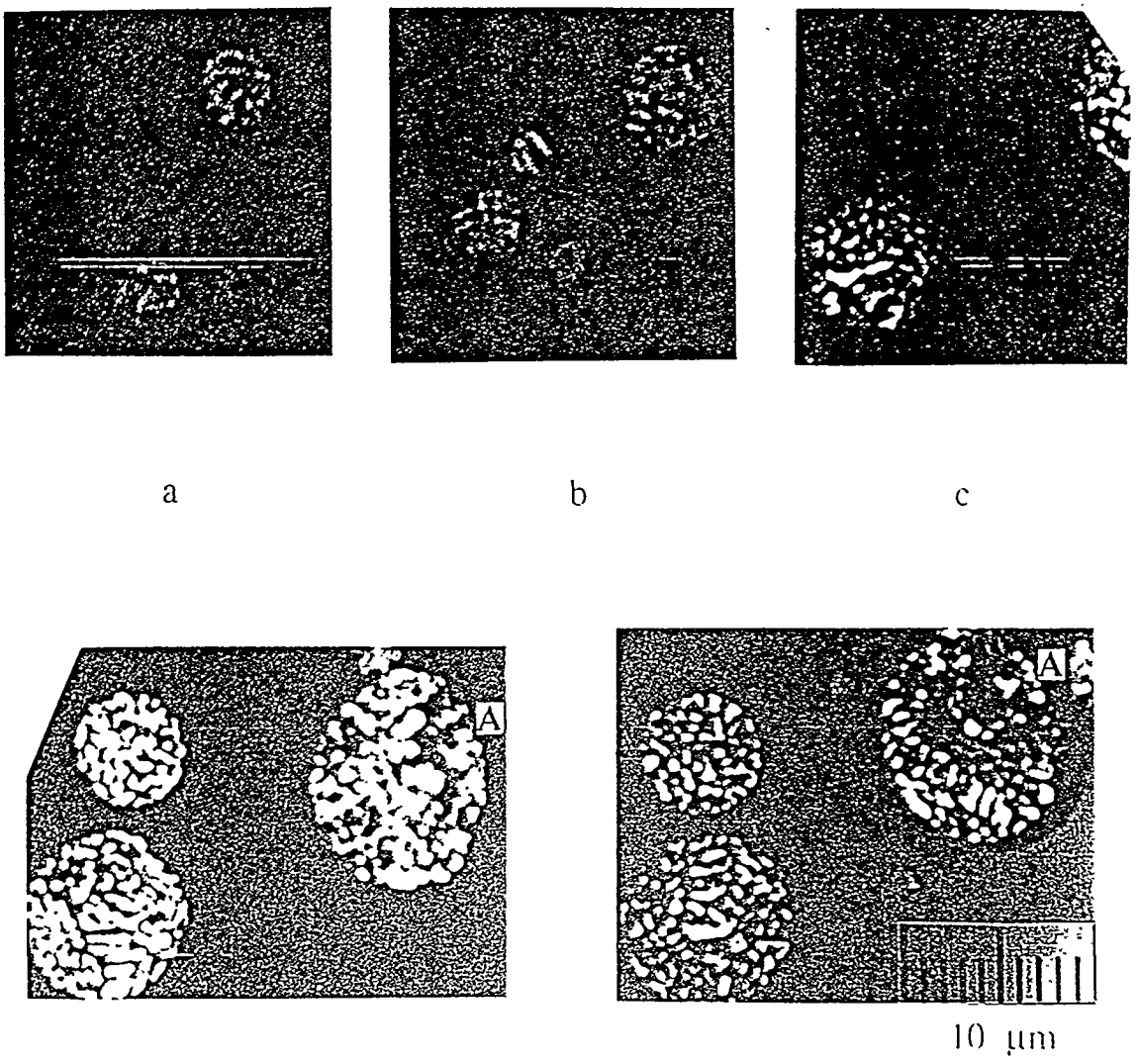

Figure 25. The cross section pictures of powder size 11.5 and 10 μm.

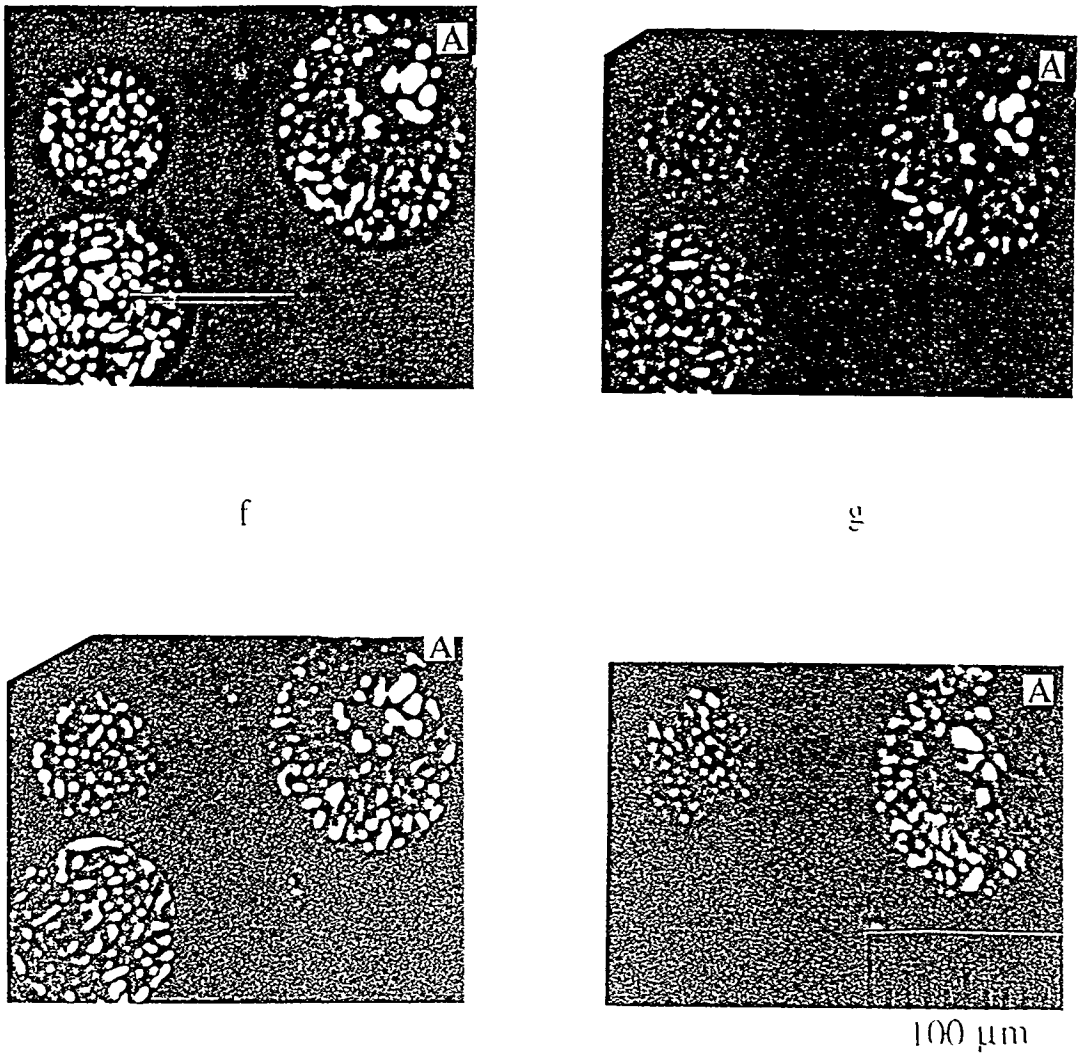

Figure 25. (continued).

5. DISCUSSION

Theoretical models for the rapid solidification of powders have been developed [Anderson and Trivedi] [30] which correlate growth microstructures with undercooling of bath to predict the selection of microstructures as a function of rapid solidification conditions. Two major constraints of this model are: 1). The application of the model to experimental data requires quantitative correlation between the undercooling, droplet size and cooling conditions in the chamber. This has not been possible so far, so that one generally obtains a qualitative prediction by assuming that the interface undercooling increases as the droplet size decreases. 2). The solidification conditions within a droplet are changing with time so that the undercooling and velocity are not constant but they vary with time. The actual variation of solidification conditions within a droplet has not been modeled quantitatively. A detailed model of heat transfer problem in a solidified droplet has been developed by Levi and Mehrabian [1] to characterize growth conditions within a powder.

5.1. Analysis of Eutectic Growth and Powder Solidification Conditions

High pressure gas atomization (HPGA) is a rapid solidification processing of powders. During this solidification processing, the cooling conditions (undercooling and velocity) in the chamber are hard to measure. However, the microstructures inside powders show the solidification process and must have some relations with solidification conditions. So the microstructure growth model can be used to obtain the powder solidification conditions. Three kinds of microstructures have been found in whole range powders. They are cellular, dendrite and eutectic. In order to obtain these powder solidification conditions two important conditions are required: 1) the microstructure must appear in whole range particles, and 2) the microstructural scales must be easy to be measured. Comparing these microstructures, the

cellular structure was found when powder size decreases to 30 μm. Although dendrite appeared at all size particles, the shape of the dendritic structure was not regular. It is not possible to measure the tip radius, primary, and secondary arms of dendrite. The eutectic structure which appeared between dendrite and cellular satisfies above two conditions.

The eutectic structure is independent of temperature gradient, so that the eutectic spacing is determined by the magnitude of interface velocity only. The JH model of eutectic growth at low velocities has been extended to high velocities by Trivedi, Magnin and Kurz (TMK) [4] using these models, it is a possible to derive the powder solidification conditions from the measurements of eutectic spacing.

Two major characteristics of eutectic growth at low velocity are : 1) $\lambda^2 V$= constant1, and 2) $\lambda \Delta T$= constant2. Both these laws are found not to be true at high velocities. At high velocities the variation in $\lambda^2 V$ with the Peclet number shows a non-constant behavior and the variation in $\lambda \Delta T$ with the Peclet number has a similar effect. However, the model JH and model TMK just show the big difference only at very high velocities, as shown in Figure 26.

The JH model shows the relations between the velocity, eutectic spacing and undercooling, as given by equations (8, 9, 10). For Al-Si alloy, the eutectic structure is irregular eutectic so that the JH model is modified to equation (11, 12, 13), with the values of the constant1=6.89×10^{-7} mm^3/s and constant2=8.9×10^{-3} mm·K.

The TMK model is more complicated than the JH model, as shown in equation (14-16). A detailed experimental study has recently been carried out by Gilgien et al. [33] in Al-Si and Al-Fe systems, who have developed a program for the calculations of dendritic and eutectic charactristics under rapid solidification conditions in these systems.

The effect of velocity on eutectic spacing in Al-Si system of two models were compared, as shown in Figure 26. For velocities < 0.3 cm/s or the eutectic spacing > 0.3 μm,

the results of two models are very close. Thus, for larger Al-Si powders the simpler JH model can be used to derive the powder solidification velocities from the eutectic spacing for powder diameter > 36 μm. The maximum velocity for Al-Si eutectic growth predicted by TMK model was 6.5 cm/s. From 0.3 cm/s to 6.5 cm/s or eutectic spacing < 0.4 μm, two models deviations were observed and increased as eutectic spacing decreases. It is indeed possible that first the temperature-dependent diffusion coefficient effect and then the high Peclet number effect may become important to give this spacing variation behavior at high velocities. The JH model can not be used to derive the powder solidification velocities for powder diameter < 36 μm. The TMK model was used to approach this high velocity solidification conditions.

The effect of undercooling on eutectic spacing in Al-Si system predicted by the two models were almost same at small undercooling conditions, as shown in Figure 27. The JH model was thus used to calculate the undercooling of these powders when undercooling was under 32 K or eutectic spacing > 0.2 μm. At large undercooling conditions, the TMK model was used.

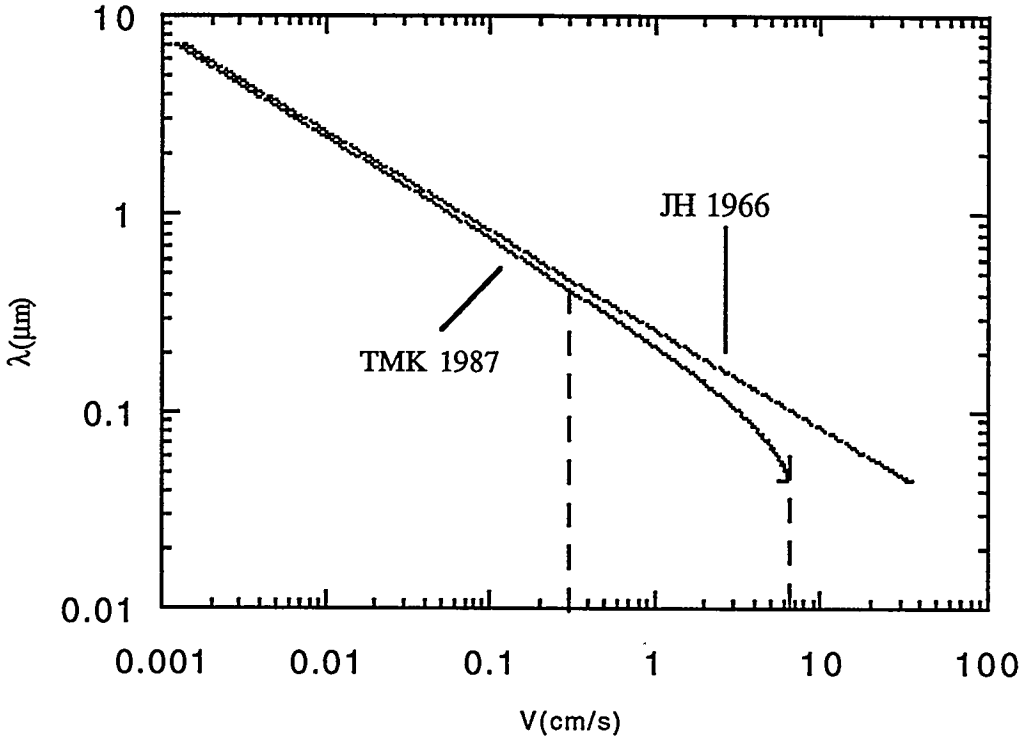

Figure 26. Calculation results on the effect of velocity on eutectic spacing in the Al-Si system. Theoretical predictions of the JH and the TMK model are shown for comparison.

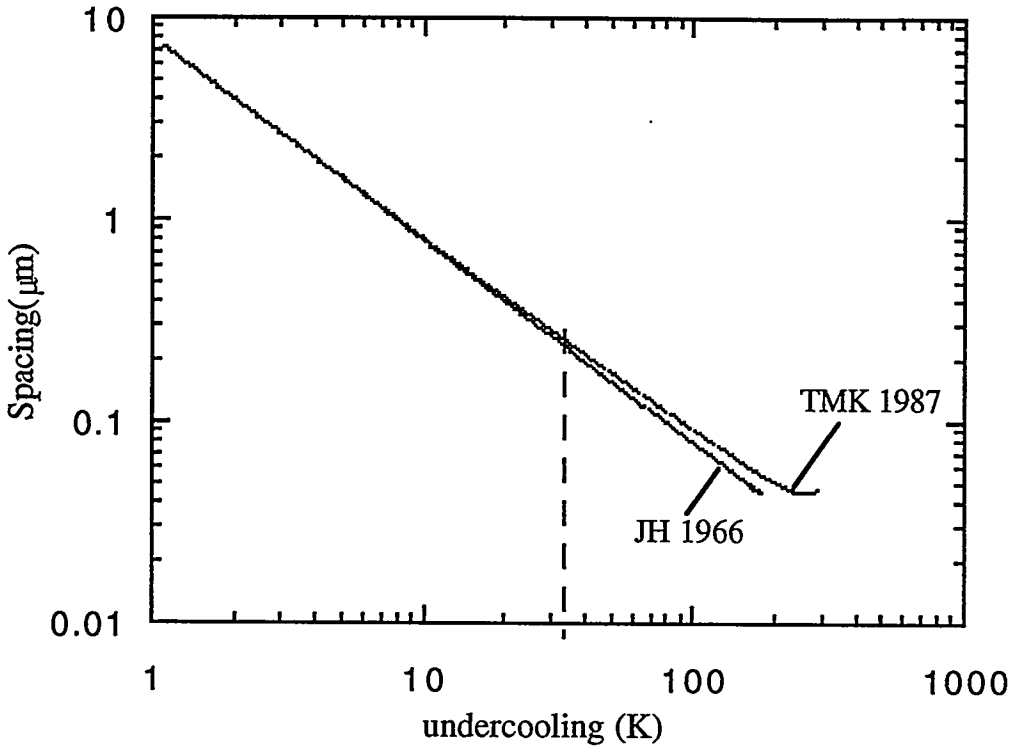

Figure 27. Calculation results on the effect of undercooling on eutectic spacing in the Al-Si system. Theoretical predictions of the JH and the TMK model are shown for comparison.

The experimental results on the eutectic spacing as a function of distance in the droplet for particle size 15 μm and 27 μm, are shown in Figure 18. From this figure, the eutectic spacing is seen to increase as the solidification proceeds further away from the nucleation region. The eutectic spacing curves of two particles are almost parallel. The average eutectic spacing of the 15 μm size powder is finer than 27 μm size powder's.

Using the theoretical model, the eutectic spacing data were converted to velocity and interface undercooling whose variations with distance in a given droplet, are shown in Figures 28, 29.

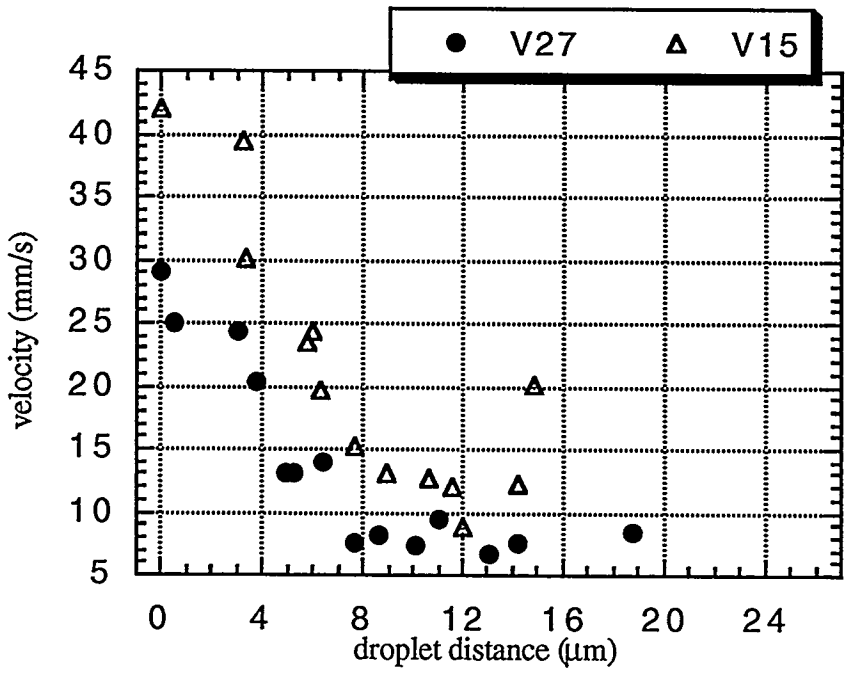

Figure 28. The interface velocity variation with droplet distance in 15 μm and 27 μm size powder .

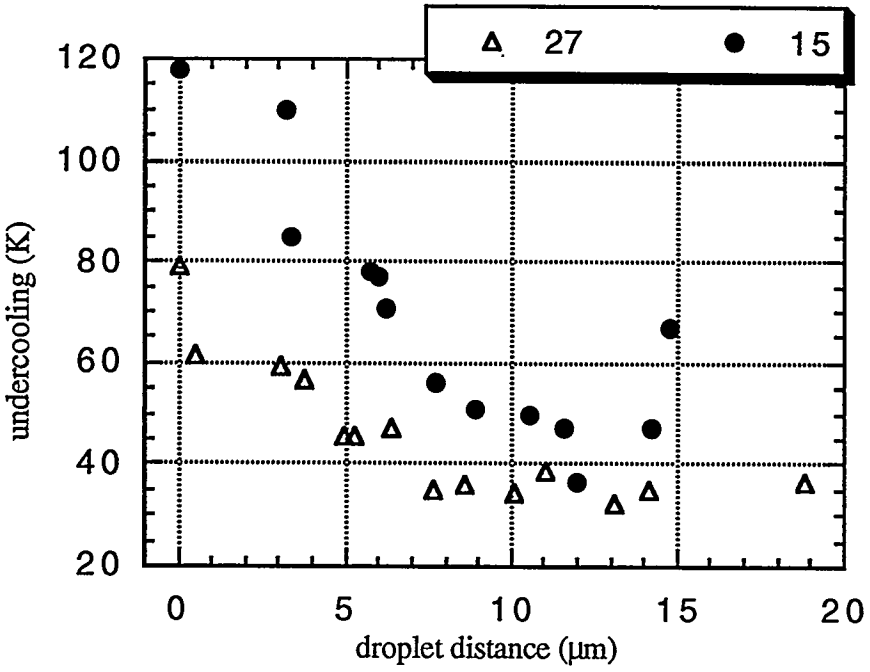

Figure 29. The undercooling variation with droplet distance in 15 μm and 27 μm size powder.

The interface growth velocities inside the droplets varied from 42 mm/s to 8 mm/s for 15 μm size powder and from 20 mm/s to 5 mm/s for 27 μm size powder. The interface undercooling varied from over 117 to 36 degrees and 79 to 30 degrees as a result of the recalescence effect in both powders. The highest velocity and undercooling for each powder were both observed at the nucleation region. The smaller the powder particle size, the larger average growth velocity and average interface undercooling. In other word, the smaller powder has lower nucleation temperature. As the melt is undercooled, the temperature gradient at the interface also varies with distance in a given droplet. Thus, the external cooling also has some influence on these powder solidification processing.

The whole range of spacing data were also converted to interface velocity and interface undrecooling which were determined as a function of powder diameter, as shown in Figure 30, 31. Vmin, Vmax, and Vave represent the minimum velocity, maximum velocity, and average velocity in these given size particles respectively. ΔTmin, ΔTmax, and ΔTave are the minimum undercooling, maximum undercooling, and average undercooling in these given size powders. However, the Vmax and ΔTmax are not real maximum velocity and undercooling inside the powder. Because the nucleation region are not included. The nucleation area is always quite fine structure and hard to resolve under SEM. In only two given size powders nucleation regions were observed and measured, as shown Vnuc and ΔTnuc in the plots.

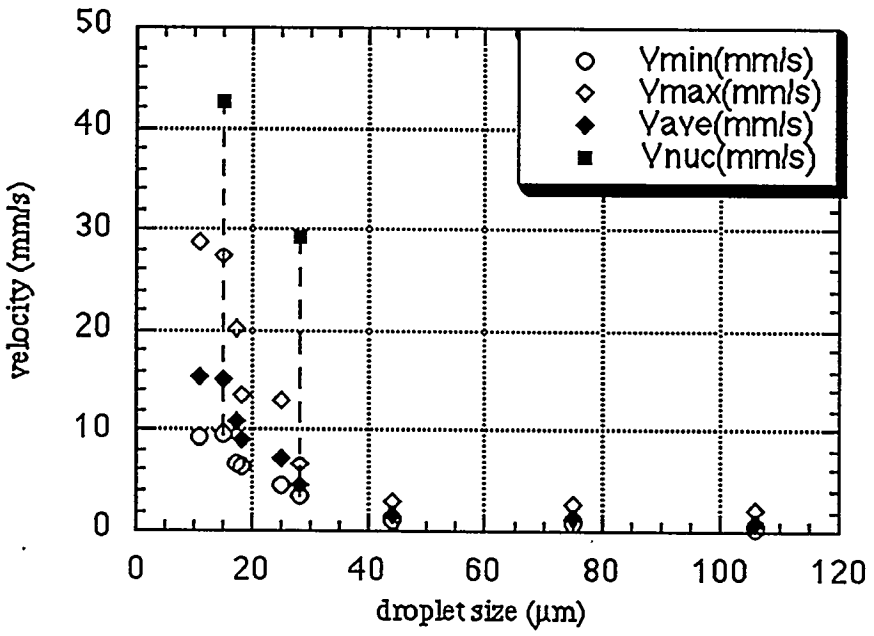

Figure 30. The interface velocity variation with particle size.

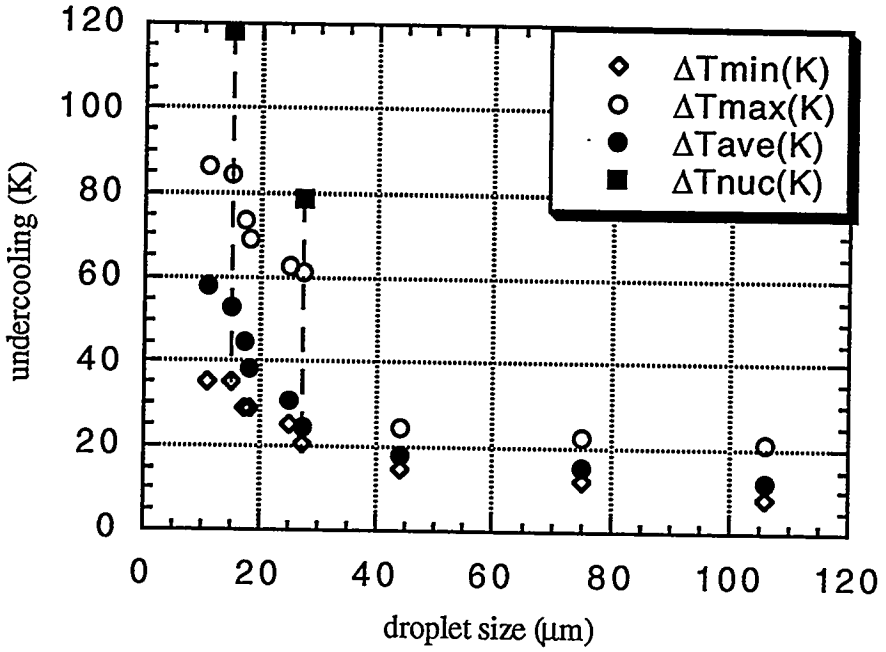

Figure 31. The interface undercooling variation with particle size.

The velocity and undercooling at the nucleation region are the real maximum values. The smaller particle size, the larger velocity and undercooling values. These solidification conditions also vary more severely in small powders. Since both cellular and eutectic structures or dendritic and eutectic structures have been found to exist in all sizes studied, the solidification must occur outside the coupled zone. The microstructures transition and Al-Si alloy coupled zone will be discussed to verify these powder solidification conditions in next section.

5.2. Microstructures Transition and Coupled Zone

These powders belong to eutectic alloy, but the microstructures of these powder always show the presence of dendritic and cellular structures besides the eutectic structure. This phenomenon can be explained by examining the coupled zone. The range of compositions and solidification conditions which give a fully eutectic microstructure are conveniently summarized by the coupled zone [16]. Figure 32 illustrates the procedure for calculating a coupled zone under undercooled melt conditions. In Figure 32 the results of the calculated interface temperatures of eutectic (T_i^e) and of dendrites (T_i^d) are given for a specific alloy composition, C_o^i. The phase that will be present will be the leading phase which has a higher interface temperature. A higher interface temperature for eutectic is a sign for pure eutectic microstructure. A higher tip temperature of dendrites indicates formation of dendrites and interdendritic eutectic. According to this criterion, a eutectic structure will be present above velocity V_i, whereas the dendritic structure will be present below the velocity V_i. One can also represent these microstructure transition conditions in terms of interface temperature. The eutectic microstructure for composition C_o^i will be present below the eutectic temperature T_i, whereas a dendritic structure will be present above the interface temperature of T_i. These results can now be represented either in the velocity-composition or the interface temperature-composition plots, as shown in Figure 32 (b and c). Such calculations, when carried out for all compositions, give the regimes of preferred steady state growth of eutectic and dendritic microstructures, as shown in Figure 32 (b and c). The superposition of microstructures on a phase diagram, given in Figure 32 (c) allows one to scan through all possible microstructures as a function of composition and interface undercooling. At the same time, the processing conditions for the required microstructure are obtained from Figure 32 (b) [17].

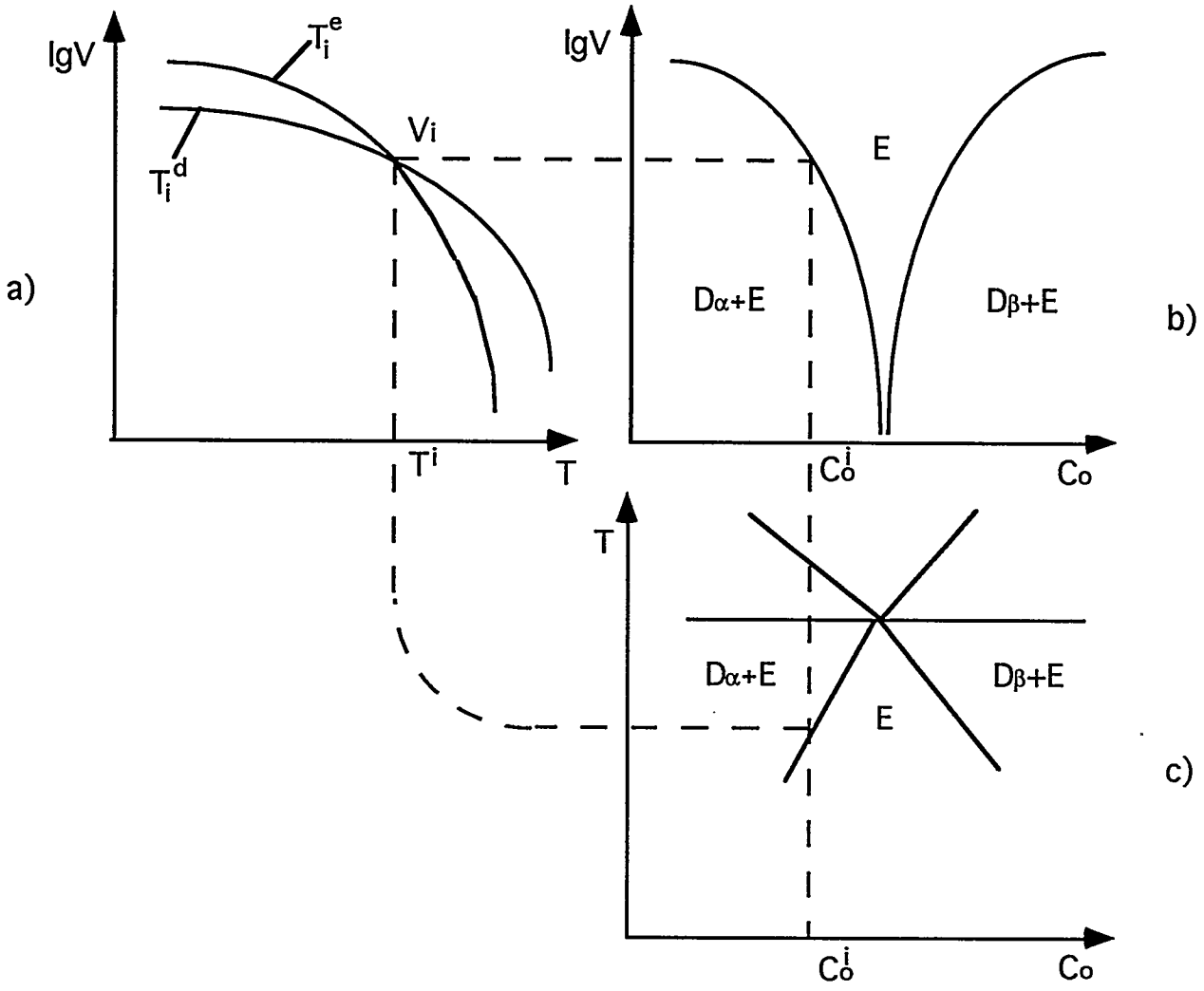

Figure 32. A schematic illustration of the procedure to develop coupled zone(a) The selection of dendrite or eutectic microstructure based on the relative interface temperatures for one composition. The super- position of results of figure (a), and of similar results for all compositions onto (b) velocity-composition map, and (c) phase diagram.

1). Eutectic growth model:

For this Al-Si alloy, the eutectic growth belongs to irregular eutectic, thus:

$$V\langle\lambda\rangle^2 = \phi^2 K_r / K_c = \text{constant1} \tag{11}$$

$$\langle\Delta T\rangle\langle\lambda\rangle = (1+\phi^2)K_r = \text{constant2} \tag{12}$$

$$\langle\Delta T\rangle / \sqrt{V} = (\phi + \frac{1}{\phi})\sqrt{K_r K_c} \tag{13}$$

Where the extremum condition, $\phi=\langle\lambda\rangle/\lambda_m$ [14].The interface temperature of eutectic structure, T obeys a law of the form [18]

$$T = T_e - \Delta T \tag{28}$$

T_e is the equilibrium eutectic temperature. The parameters of Al-Si eutectic composition system are shown in Table 3. These parameters were substituted into equations (6, 7) to get constants K_r and K_c. Then K_r and K_c were substituted into equations (11, 12, 13) to obtain constant1=6.89×10^{-7} mm^3/s, constant2=8.9×10^{-3} mm·K.

2). The dendritic growth model:

The interface temperature, or undercooling, for dendritic growth in an undercooled melt condition (free growth) [20] is given by:

$$\Delta T = [\frac{k\Delta T_0 Iv(P)}{1-(1-k)Iv(P)}] + [\frac{2\Gamma}{R}] + [\frac{\Delta H}{c_l} Iv(P_t)] \tag{29}$$

$$T = T_l - \Delta T \tag{30}$$

Where T is the interface temperature of dendritic structure, T_l is the liquidus temperature.

Parameter Name	Parameter Value
Diffusion Coefficient (D)	5×10^{-9} m^2/s
Length of Eutectic Tie-line (C')	98.2 wt %
Eutectic Growth Series Term (P')	8.9×10^{-3}
α Phase Fraction ($f\alpha$)	0.873
β Phase Fraction ($f\beta$)	0.127
α Phase Liquidus slope ($m\alpha$)	7.5 K/wt %
β Phase Liquidus slope ($m\beta$)	17.5 K/wt %
Gibbs-Thomson Coefficient ($\Gamma\alpha$)	1.96×10^{-7} Km
Gibbs-Thomson Coefficient ($\Gamma\beta$)	1.7×10^{-7} Km
Angle of α Phase ($\theta\alpha$)	30°
Angle of β Phase ($\theta\beta$)	65°
Extremum Condition(ϕ)	3.2

Table 3. The parameters of Al-Si alloy eutectic composition system.

The interface temperature/growth rate curves of the eutectic, Al dendrite and Si dendrite for compositions near the eutectic composition were plotted in the same rectangular axes, as shown in Figure 33. Then, the cross points of these curves were plotted onto the phase diagram, as shown in Figure 34.

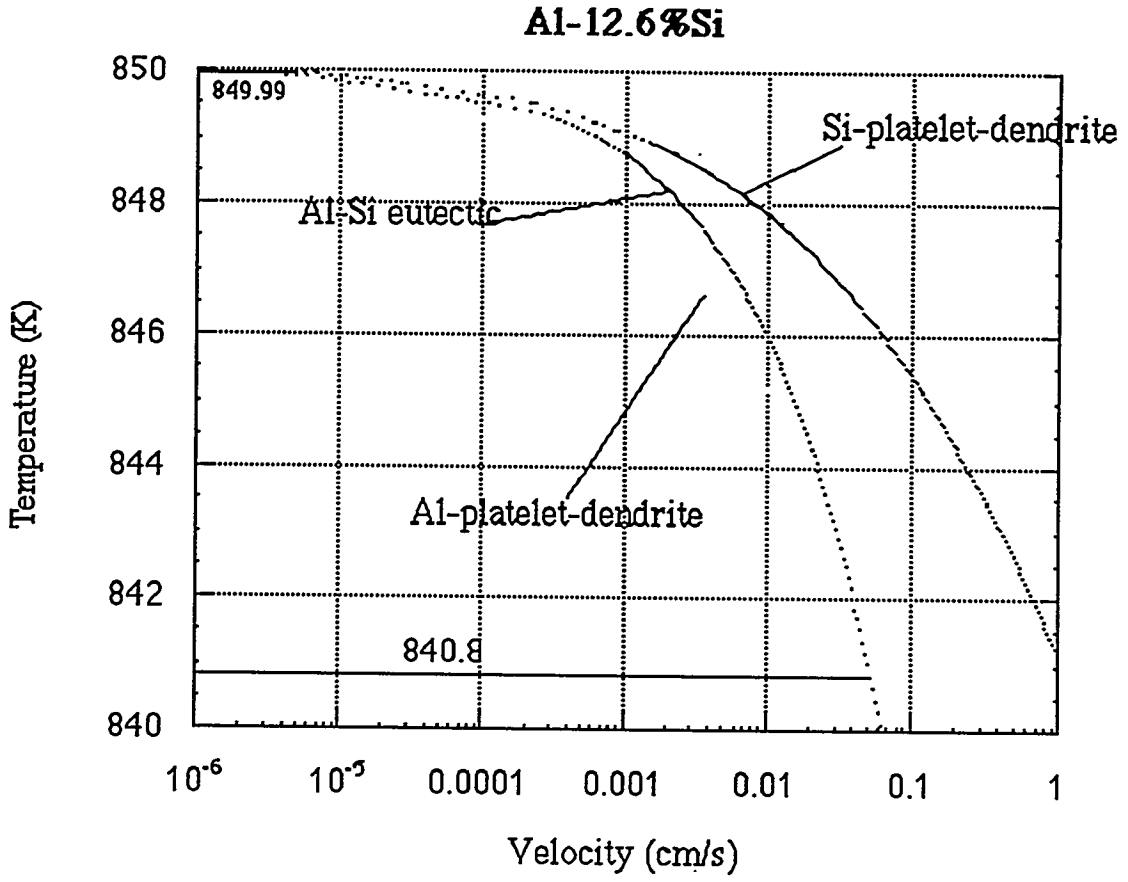

Figure 33. The interface temperature/growth rate curves for the competing morphologies (Al-Si eutectic, Al platelet dendrite and Si platelet dendrite) at Al-12.6% Si composition.

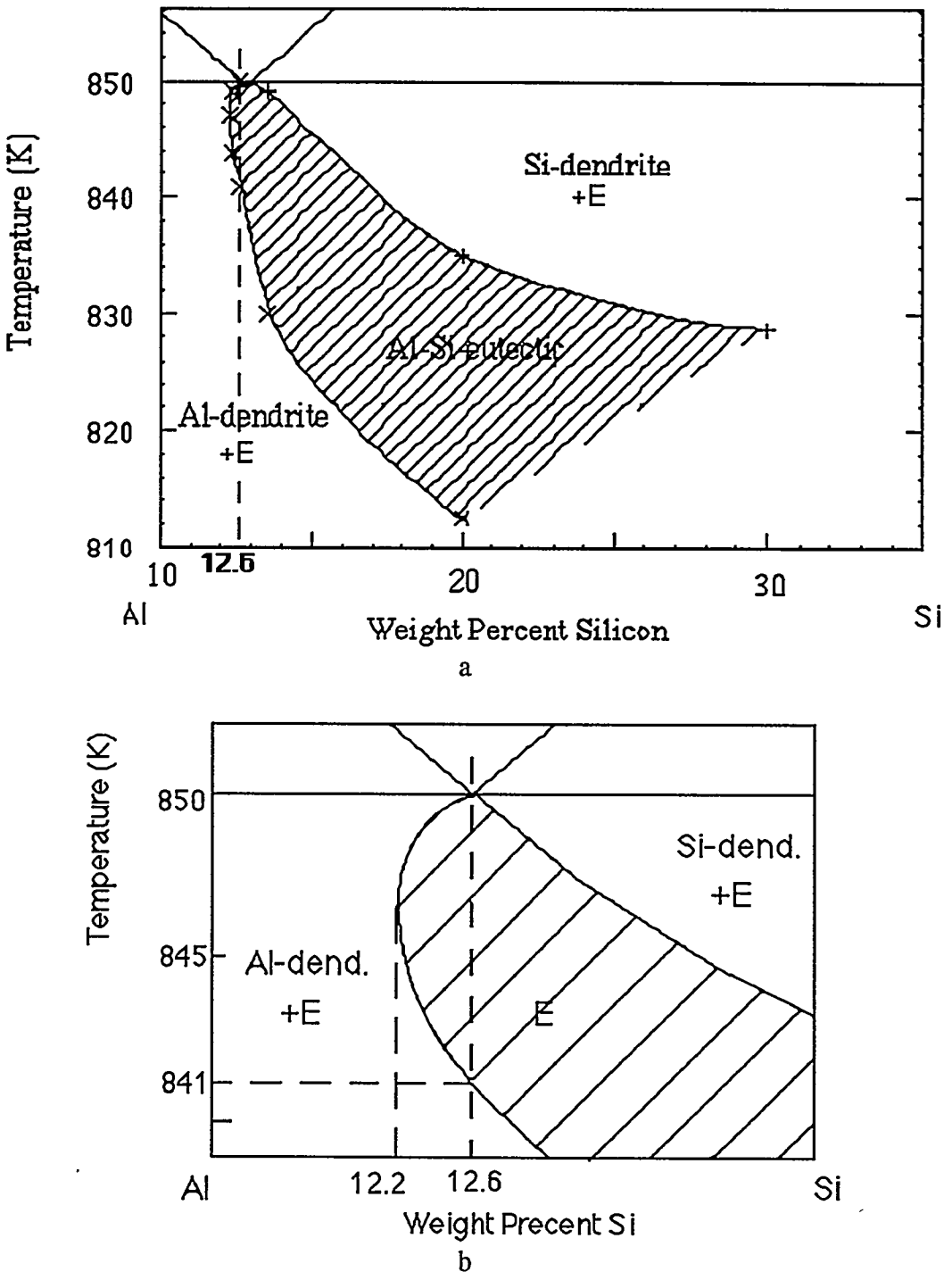

Figure 34. a) Al-Si coupled zone, b) maginfied coupled zone area at eutectic melting point.

The eutectic coupled zone area of Al-Si alloys has been calculated, as shown in Figure 34. The shaded region is the coupled zone area. If an Al-Si alloy can be supercooled into this shaded region, it will be found to solidify with eutectic structure; if it is outside this shaded region, it will have a planar or cellular or dendritic growth with eutectic structures in the interdendritic region. Since dendritic, cellular and eutectic structures were found in all different size powders studied. That interface temperature of these range of powders must be outside the eutectic coupled zone area during the solidification processing. Figure 34 shows that the maximum undercooling for the coupled zone is 9 K.

The coupled zone diagram can be used to compare with the powder solidification conditions which were calculated by using the JH and TMK models. First, the maximum undercooling of each size powder were obtained from Figure 31. They must be found near the nucleation region. Then they were converted to the interface temperature by equation (29). The interface temperatures were found to vary from 731 K to 838 K, which were outside the eutectic coupled region. Thus, single phase Al-dendrites or cells plus eutectic structure were observed inside the powders. These results show that the JH and TMK models can be used to determine rapid solidification conditions inside the powders.

5.3. The Calculation of the Undercooling Inside Powder by Newtonian Thermal History Model:

The variation of the interface undercooling inside 27 μm size powder is also calculated by using the Newtonian thermal history model. The initial undercooling is chosen the same as the eutectic spacing calculation, 79 K. Other parameters are shown in Table 4.

The dimensionless temperature θ for different interface inside powder can be obtained from equations (1~4). The interface undercooling can be converted by using the relationship

$\Delta T=-\Delta H\theta/C_L$. The results of thermal history calculation are compared with eutectic spacing data, as shown in Figure 35. The thermal history model qualitatively agrees with the general behavior exhibited by experimental results. The quantitative agreement, however, is not good in particle diameter range between 1 and 5 μm. Also, the calculation were carried out by adjusting the parameters, Bi and K_M, so as to obtain a better fit with the experimental results.

Parameter Name	Parameter Value
Heat Fusion (ΔH_M)	135.87 cal/g
Specific Heat Liquid(c_L)	0.254 cal/g°C
Specific Heat Solid (c_S)	0.209 cal/g°C
Thermal Diffusivity (α_L)	$3.1X10^{-5}$ m^2/s
Melting Temperature (T_M)	850 K
Stefan Number (Ste for T_G=300K)	1.18
Powder Radial (r_o)	27 μm
Biot Number (Bi)	0.002
Kinetic Parameter (K_M)	0.074

Table 4. Parameters for Newtonian model.

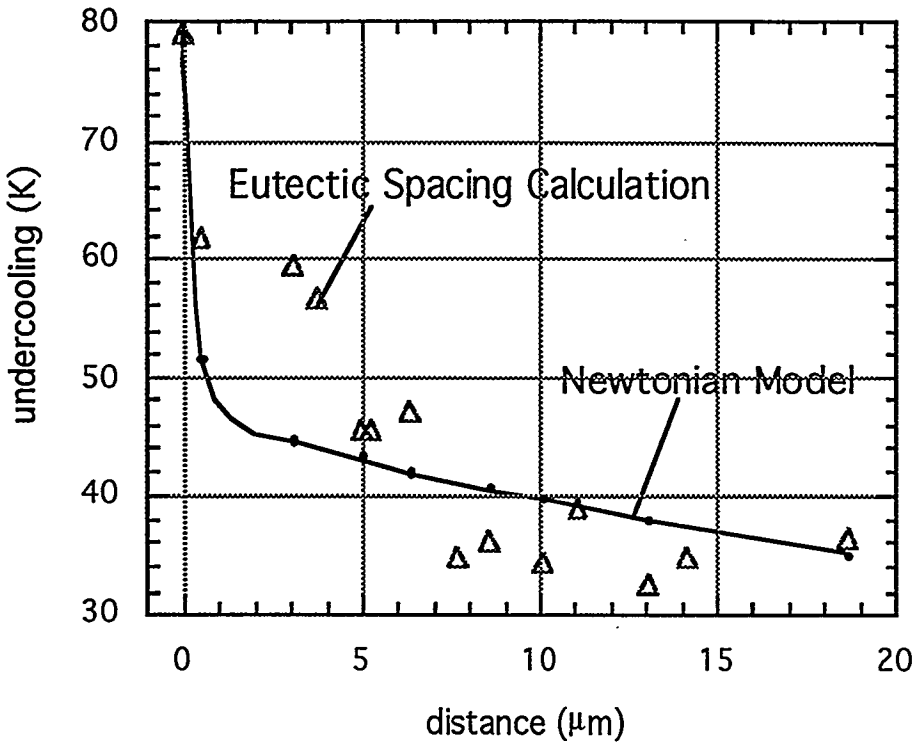

Figure 35. The interface undercooling for 27 μm size powder, one is obtained from eutectic spacing, another is obtained from Newtonian model.

5.4. Hardness, Particle Size and Microstructural Spacing

The relation between particle size and hardness is shown in Figure 23. The hardness decreases with particle size decreasing, when powder diameter is larger than 40 μm. From 40 μm to 20 μm, the hardness increases with particle size decreasing. It is hard to measure the powder diameter less than 20 μm.

The finer grain size, the higher hardness. The eutectic structure is the hardest inside the powder. The cellular structure is harder than dendritic.

The microstructure transition map (Figure 15) shows that the volume of dendritic structure increases from diameter 106 μm to 38 μm, and the volume of eutectic structure

decreases at this range. But the average eutectic spacing in this range particles changes just a little. The volume fraction change of microstructures has more affect to hardness than eutectic spacing change at this range size powders. So the hardness of the powder decreases from 120 μm to 40 μm. From 40 μm to 20 μm, the volume of the dendritic structure decreases very severely. At the same time, the cellular structure appears and its volume fraction increases as the diameter decreases. The cellular spacing is much smaller than dendritic spacing, and it decreases sharply, as shown in Figure 22. The volume fraction of the eutectic structure, however decreases very slowly. The powder hardness was compared with microstructural spacing and volume fraction, as shown in Figure 36 (a, b). The eutectic spacing changes significantly, but the volume fraction of the eutectic structure is quite low. At this range size powders (40 μm ~ 20 μm), the volume of the cellular structure and cellular spacing are the keys to the increase in the hardness.

So the average hardness of these powders must be as a function of the volume fraction of these three microstructures and the spacing size of each microstructures, according to the following equations:

$$H = f_e \cdot h_e + f_d \cdot h_d + f_c \cdot h_c \tag{31}$$

$$f_i = f(D) \tag{32}$$

$$h_i = f(s_i(D)) \tag{33}$$

H is the hardness of the powder; f_e, f_d and f_c are the volume fraction of the eutectic, dendritic, and cellular structures, which are also factions of the particle diameter (D); h_e, h_d and h_c are the hardness of the eutectic, dendritic, and cellular structure, they also are factions of the microstructure spacing (s_i) and the particle diameter (D).

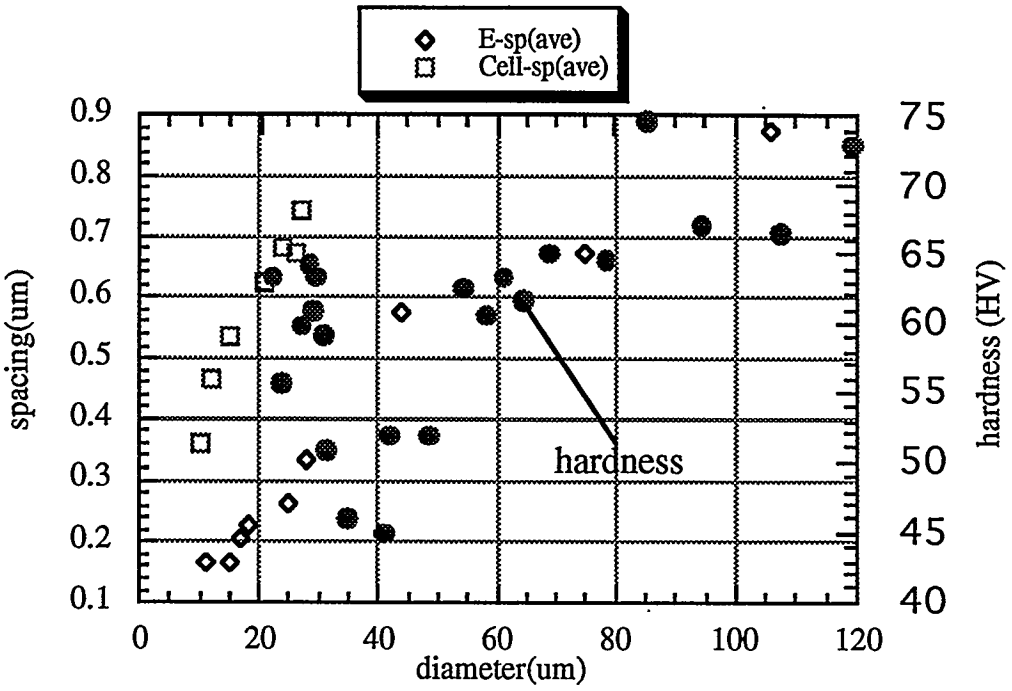

a

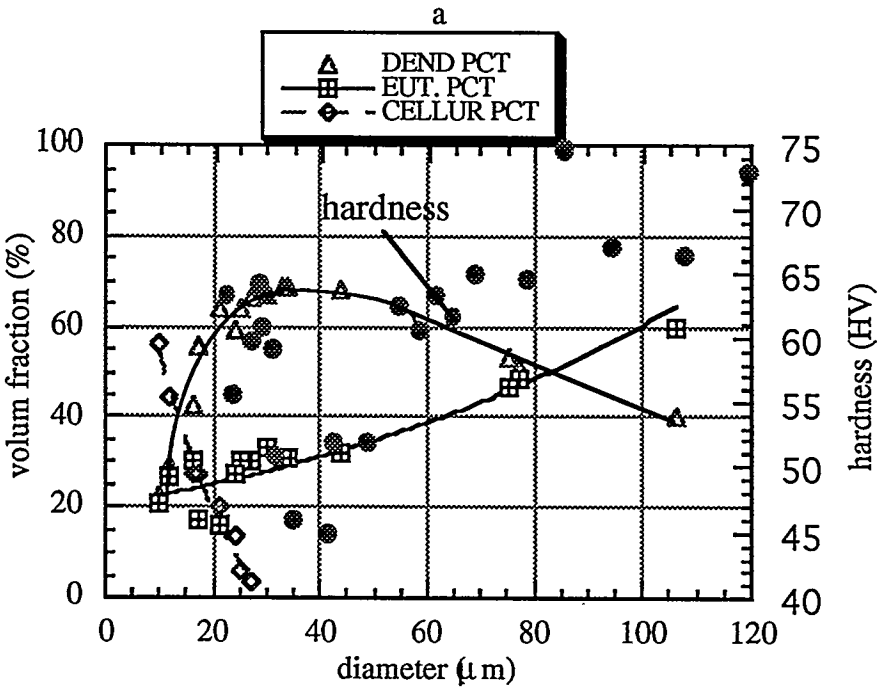

b

Figure 36. a. Hardness and microstructural spacing, b. Hardness and volume fraction.

The epoxy hardness is round 17 HV. The hardness of these powders is much higher than the hardness of the epoxy. The epoxy is not hard enough. During powder hardness test, the powder must be pressed into epoxy. The diamond hardness test mark on the powder surface is not very full. So the test hardness value of the powder is higher than the real value. This phenomenon is more serious in small powder. The present data shows the general trend of hardness variation with microstructure.

5.5. Nucleation Region

So far two kinds of nucleation region have been already found from the series cross section pictures of diameter 19 μm and 11.5 μm size powders. They were: 1) self-start nucleation region, and 2) second-start nucleation region. If melt solidifies at one or more points and crystal grow continually from these points, the nucleation region in this kind of droplet is the self-start nucleation region, as shown the area 'A' in Figure 24 (g). If melt meet some small particles before nucleating, the nucleation will be around these small particles and crystal will grow from the surface of small particles. This kind of nucleation belongs to the second-start nucleation, as shown the area 'A' in Figure 25 (d).

For these two kinds of nucleation regions, measurements of the microstructure scales are different for the calculation of the nucleation region solidification conditions. For the self-start powder, the measurement was carried out at that first solidified region; For the second-start powder, the measurement was carried out at the outside of that first solidified small particle. The microstructures of the nucleation region could be planar, cellular, and some eutectic structures. They will depend on the nucleation cooling condition.

6. CONCLUSION

From the experimental study of atomized Al-Si alloy powders, the following conclusions can be made concerning the solidification of powders, powder microstructural transitions, and powder micro-hardness property that are used to optimize powder in the intelligent processing of materials.

(1) The powder rapid solidification conditions (undercooling and velocity) have been calculated by using TMK and JH's eutectic growth models from the eutectic spacing measurements inside these powders. For this Al-Si system, the TMK model is used when the particle size less than 36 μm. The JH model can be used for larger size powders.

(2) The growth velocity and interface undercooling as a function of droplet distance in a given particle has been calculated. The highest value of the solidification conditions are found near the nucleation region.

(3) The interface undercooling and velocity, as a function of powder size, have been measured over the whole range particles. The highest value of the solidification conditions are found in the smallest particle.

(4) Rapidly solidified powders of Al-12.6 wt pct Si exhibit three characteristic microstructures: eutectic, dendrite, and cellular. The cellular structure appears as the powder size decreases to 30 μm. The volume fractions of these three microstructures as a function of powder diameter have been measured.

(5) The interface undercooling and velocity inside powder have also been calculated by using the Newtonian thermal history model. The results agree qualitatevely with the eutectic spacing calculation.

(6) The hardness property of the powder size from 20 μm to 120 μm are also as functions of microstructural spacings and particle size. 40 μm ~ 35 μm size powders show the minimum hardness, 45 HV. Decreasing or increasing powder size from this point, the hardness is found to increase. It is hard to measure the small powder's hardness property, so the maximum hardness can not be determined preciesly.

(7) Two kinds of nucleation regions are found in these powders. One is self-start nucleation region. Another is second-start nucleation region. The first one is the most common nucleation event. The second-start nucleation region is observed in about 30% of powders.

7. REFERENCES

1. C. G. Levi and R. Mehrabian, Metall. Trans. A, 1982, vol. 13A, p221.
2. C. G. levi, Metall. Trans. A, 1988, vol. 19A, p699.
3 W. J. Boettinger, L. Bendersky and J. G. Early, Metall. Trans. A, 1986, vol. 17A, p781.
4. R. Trivedi, P. Magnin and W. Kurz, Acta Metall., 1987, vol. 35, No. 4, p971.
5. W. Kurz and R. Trivedi, Metall. Trans. A, 1991, vol. 22A, p3051.
6. B. Wei and D. M. Herlach, J. Mater. Sci. letter, 1993, 12, p1774.
7. B. Wei and D. M. Herlach, Mater. Sci. and Engi., 1993, A173, p357.
8. S. C. Sharma, T. Volkmann and D. M. Herlach, Mater. Sic. and Engi., 1993, A171, p169.
9. Y. Wu, T. J. Piccone, Y. Shiohara and M. C. Flemings, Metall. Trans. A, 1987, vol 18A, p915.
10. Shu-Zu Lu, J. D. Hunt, P. Gilgien and W. Kurz, Acta. Metall., 1994, vol. 42, No. 5, p1653.
11. Shu-Zu Lu and J. D. Hunt, J. Crystal Growth, 1993, 123, p17.
12. M. Pierntoni, M. Gremand, P. Magnin, D. Stoll and W. Kurz, Acta Metall. Mater., 1992, vol. 40, No. 7, p1637.
13. W. Kurz and R. Trivedi, The American Society of Mechanical Engineers, 1989, MD-vol. 14, p47.
14. M. carrard, M. Gremand, M. Zimmermann and W. Kurz, Acta. Metall. Mater., 1992, vol. 40, p983.
15. S. C. Gill, M. Zimmermann and W. Kurz, Acta. Metall. Mater., 1992, vol. 40, p2895.
16. W. Kurz and D. J. Fisher, International Metals Reviews, 1979, No. 5&6, p177.
17. R. Trivedi and W. Kurz, International Processing of Materials, 1990, p177.

18. C. G. Levi and R. Mehrabian, Metall. Trans. A, 1982, vol. 13A, p13.

19. J. Lipton, Kurz, and Trivedi, unpublished research, 1986.

20. E. Schleip, D. M. Herlach and B. Feuerbacher, Europhys. Lett., 1990, 11, p751.

21. K. A. Jackson and J. D. Hunt, Trans. Met. Soc. AIME, 1966, 236, p1129.

22. W. Kurz and D. J. Fisher, "Fundamentals of Solidification", Trans. Tech. Publications, 1984.

23. R. Trivedi and W. Kurz, International Materials Reviews, 1994, vol. 39, No. 2, p49.

24. D. Bensimon, P. Pelce and B. I. Shraiman, J. Phys. A, 1987, vol. 48, p2081.

25. A. Papapetrou, Z. Kristallogr., 1935, 92, p89.

26. Y. Saito, G. Goldberg-Wood and H. Müller-Krumbhaar, Phys. Rev. Lett., 1988, A38, p2148.

27. J. D. Ayers and I. E. Anderson, "Method for Generating Fine Sprays of Molten Metal for Spray Coating and Powder Making," U.S. Patent No. 4,619,845, October 28, 1986.

28. I. E. Anderson and B. B. Rath, "Rapid Solidification of Copper-Based Alloys," in:Rapidly Solidified Crystalline Alloys, S. K. Das, B. H. Kear, and C. M. Adam, Eds., 1985, TMS-AIME, Warrendale, PA, p219.

29. I. E. Anderson, H. Morton and R. S. Figliola, " Fluid Flow Effects in Gas Atomization Processing," in: Physical Chemistry of Powder Metals Production and Processing, W. M. Small, ed., 1989 TMS, Warrendale, PA, p229.

30. Anderson, I. E. and Trivedi, R., unpublished work, 1992, Ames Laboratory, Ames, IA.

31. R. M. German, Library of Congress Cataloging-in-Publication Data, 1994, 2nd ed., "Powder Metallurgy Science".

32. R. Grugel and W. Kurz, Metall. Trans. A, 1987, vol. 18A, p1137.

33. Ph. Gilgien, The Dendritic and Eutectic Solidification Programs, 1993.

34. Thaddeus B. Massalski, Hiroaki Okamoto, P. R. Subramanian, and Linda Kacprzak, ASM, "Binary Alloy Phase Diagrams", 1990, 2nd edition, vol. 1, p211.

8. ACKNOWLEDGMENTS

First, I need to thank Dr. Rohit Trivedi for giving me this chance to work in his group. Without his help and guidance, this project would have never been made to fruition. Almost three years working under Dr. Trivedi, I am very impressed on his vast knowledge, philosophy on learning, and patience.

Second, I would also like to thank my other graduate committee members of Dr. Iver Anderson and Rolando Flores for their help and support of my thesis work. Additional thanks to Mark Eshelman, Seung Hoon Han, John Mason, and Fran Labbs for their help.

Next I appreciate Dr. W. Kurz and Dr. Ph. Gilgien providing the coupled zone program.

Final thanks goes to Ames Laboratory and the Department of Energy for the project funding and the research facilities.

This work was performed at Ames Laboratory under contract No. W-7405-eng-82 with the U.S. Department of Energy. The United States government has assigned the DOE Report number IS-T 1756 to this thesis.